Chapter 6

Numerical Examples

6.1 Sloshing in a Rectangular Tank

In this section we perform a study of sloshing in a three-dimensional tank subjected to external excitation. The objective of this exercise is to assess the capabilities of the space-time finite element formulation as a method of handling deforming domain problems. The origins of the current problem can be traced to experiments by Muto et al. [53]. Subsequently the problem has been used to evaluate the performance of various deforming domain numerical methods, including ALE [10,11]. The continuing interest in the problem stems from its many potential applications. A priori knowledge of the movements of the fluid under given excitation is often needed to predict forces acting on the structure supporting the fluid. This in turn enables us to e.g. estimate dynamical behavior of a spacecraft due to the motion of the propellant.

6.1.1 Horizontal excitation

First we model a sloshing container subjected to horizontal excitation experimentally examined in [53].

The problem is stated as follows:

- Water fills the initially rectangular $W \times H \times D$, ($W = 0.8\,\mathrm{m}, H = 0.1\,\mathrm{m}$ and

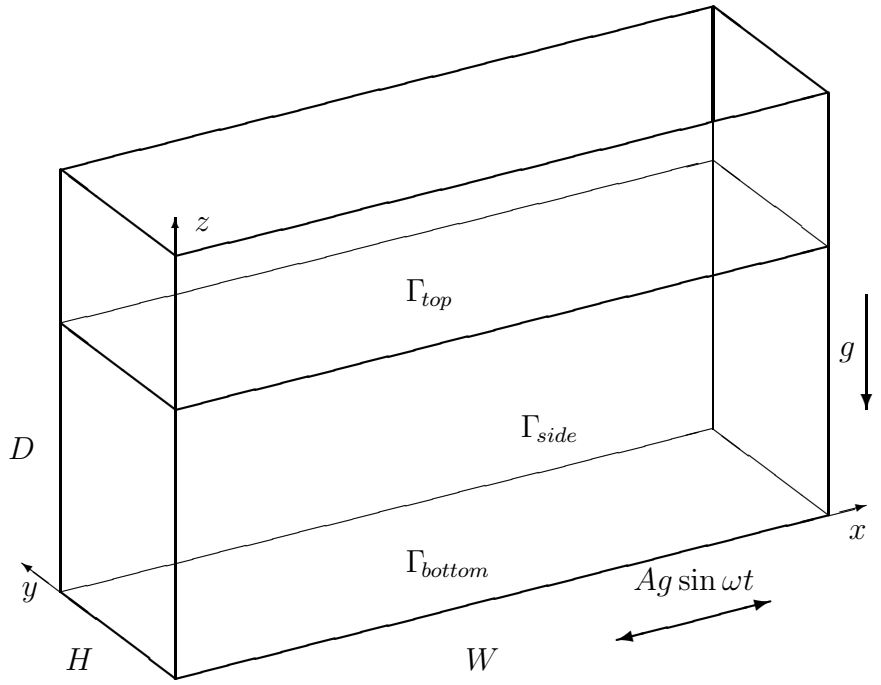

Figure 6.1. Horizontally oscillating tank: domain description.

$D = 0.3\,\mathrm{m}$) domain as shown in Figure 6.1. In keeping with the previous numerical simulations, boundaries Γ_{bottom} and Γ_{side} allow slip in the direction tangent to the surface. It is hoped that this idealization will not significantly affect the motion of a low-viscosity fluid. The boundary Γ_{top} is left free, and moves with the normal component of the fluid velocity at the surface. The normal directions are computed using the consistent normal approach of [54].

- The external forces acting on the fluid consist of a constant gravitational acceleration of magnitude $g = 9.81\mathrm{ms}^{-2}$ and of a sinusoidal horizontal excitation $Ag\sin\omega t$ with $A = 0.01$ and $\omega = 2\pi f,\ f = 0.89\,\mathrm{Hz}$.

- At each time level, the domain is discretized using a finite element mesh with 1,305 nodes and 800 brick trilinear elements. In the resulting space-time mesh,

	Dimensional	Non-dimensional
Lengths	$D = 0.3\,\mathrm{m}$	$\tilde{D} = 1.0$
	$H = 0.1\,\mathrm{m}$	$\tilde{H} = 0.3333$
	$W = 0.8\,\mathrm{m}$	$\tilde{W} = 2.6667$
Frequency	$f = 0.89\mathrm{s}^{-1}$	$\tilde{f} = 0.156$
Acceleration	$g = 9.81\mathrm{ms}^{-2}$	$\tilde{g} = 1.0$
Viscosity	$\nu = 1.0 \times 10^{-6}\mathrm{m}^2\mathrm{s}^{-1}$	$\tilde{\nu} = 1.943 \times 10^{-6}$
Time step	$\Delta t = 0.0187\mathrm{s}$	$\Delta\tilde{t} = 0.107$

Table 6.1. Horizontally excited tank: parameters.

each time slab consisting of 2,610 nodes and 800 quadrilinear four-dimensional brick elements.

- The problem is non-dimensionalized in a way described in [10]. The full set of dimensional as well as non-dimensional parameters is summarized in Table 6.1.

- Computations in this section use a GMRES solver with diagonal scaling. Krylov space size of 20 was chosen, and the maximum number of outer GMRES iterations is set to 10. At each time step, an average of 3 non-linear iterations were required to meet the convergence criterion. The simulations were done in 64-bit precision on the CM-5 computer.

The sloshing motion is initiated as soon as the excitation is applied. The excitation frequency is designed to induce the first mode of wave motion in the x direction, i.e., the motion with a wavelength approximately equal twice the width of the tank W. This motion is indeed produced, and virtually no three-dimensional effects, nor any higher wave motion modes, are visible. The time histories of the height of the wave at the two opposite walls perpendicular to the x-axis are shown in Figures 6.2 and 6.3. For the first ten periods of excitation the measured wave height is quite close to the one reported in [10], with the difference not exceeding 4%. After the initial ten periods the

excitation in [10] is removed, and the wave growth stops. In the current simulation we continued the excitation, matching the experimental conditions reported in [53]. The maximum upward wave deflection reaches more than double of the original height, and the occurrence of second frequency is clearly visible in the wave height envelope. That transient is decaying extremely slowly, as the damping in the system, provided by the fluid viscosity, is very low. The results presented here do not extend to the eventual quasi-steady state of periodic sloshing, but it may be extrapolated that the final minimum and maximum vertical displacements of the fluid at the wall should reach 1.6 and 0.75, respectively, of the undisturbed wave height. The quasi-steady wave height for the excitation frequency of 0.89Hz measured in [53] is 1.53. The six frames in Figure 6.4 show the deformed finite element mesh at equally spaced instant within one period of oscillations. The amplitude of the sloshing at this point is close to the expected quasi-steady state. The corresponding six frames in Figure 6.5 show the velocity field at the plane of symmetry $y = H/2$.

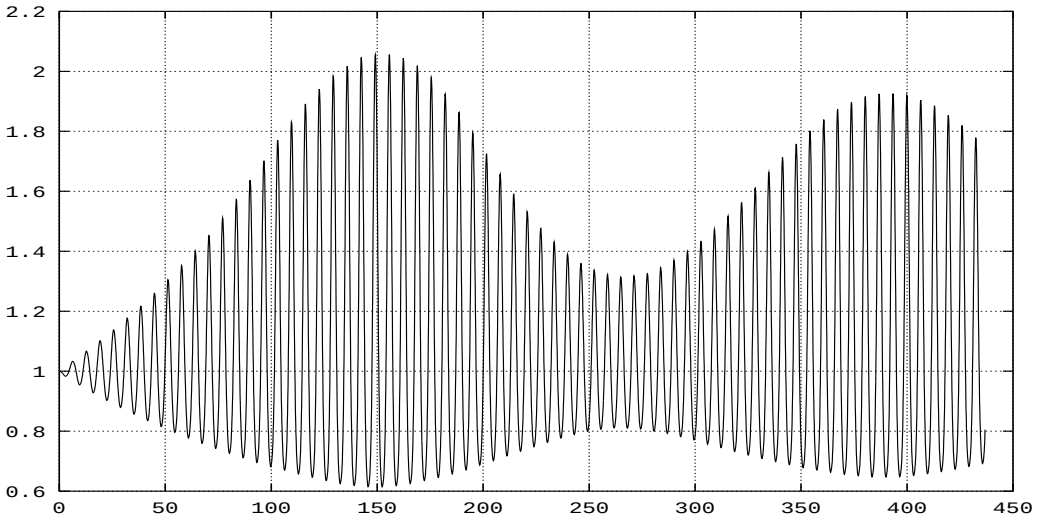

Figure 6.2. Horizontally excited tank: time history of the wave height at the $x = 0$ wall.

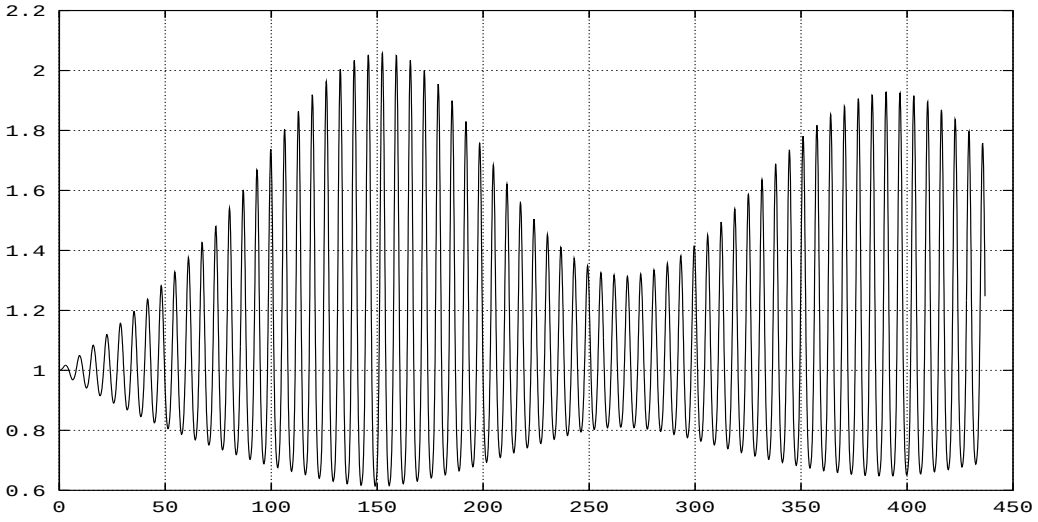

Figure 6.3. Horizontally excited tank: time history of the wave height at the $x = W$ wall.

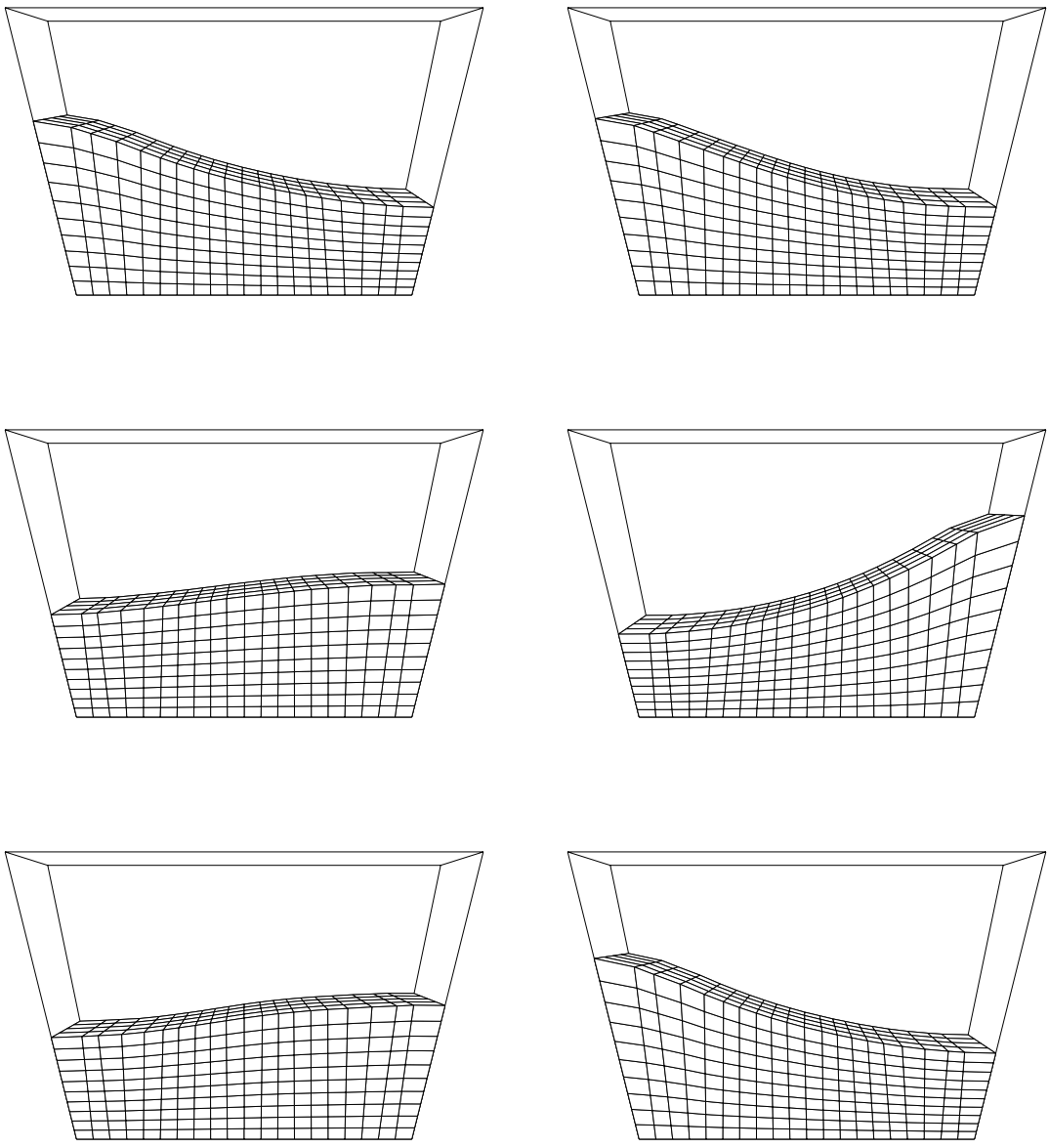

Figure 6.4. Horizontally excited tank: finite element mesh at $t = 314.77, 316.06$ (top row), $t = 317.34, 318.63$ (middle row), and $t = 319.91, 321.20$ (bottom row).

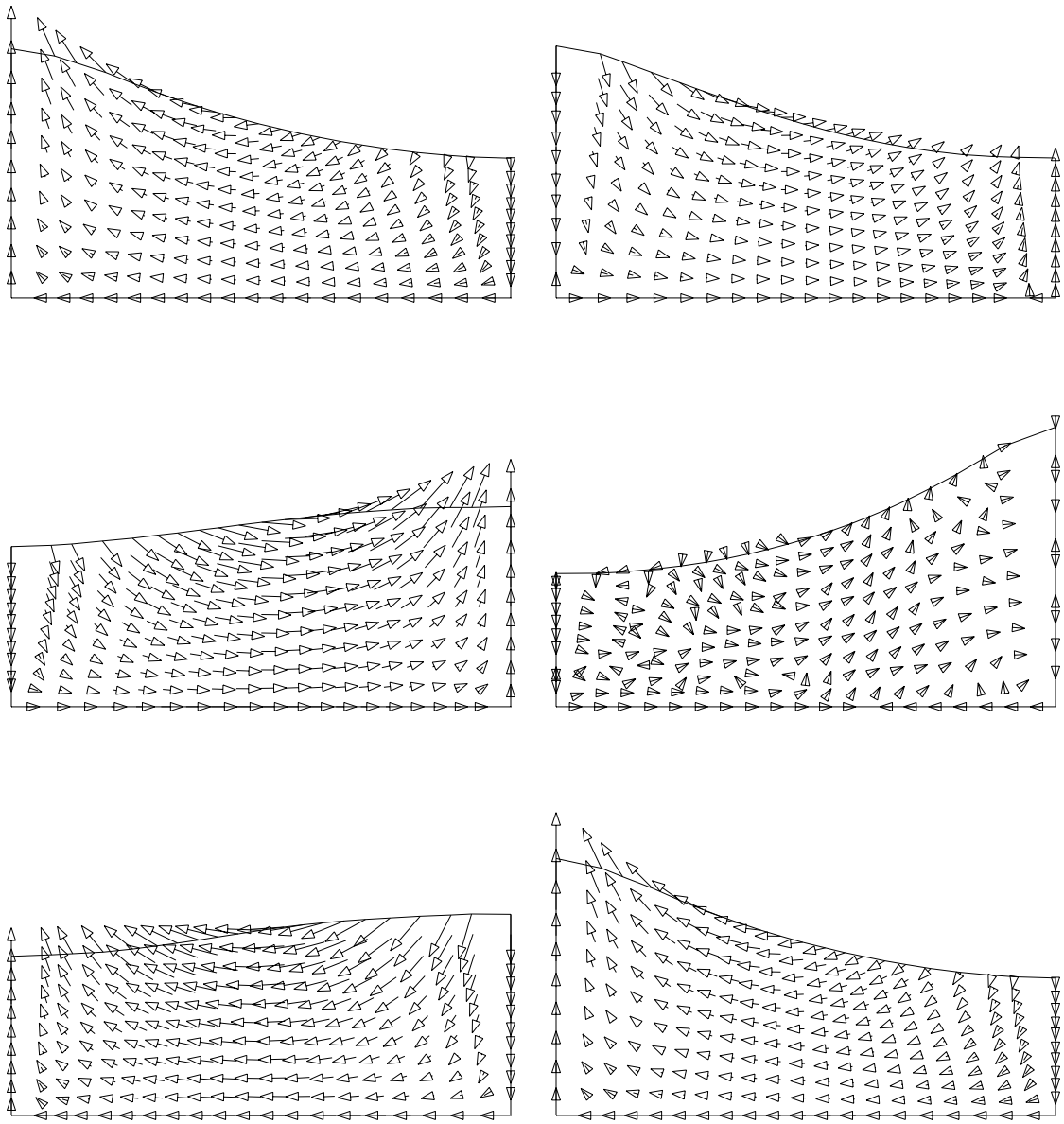

Figure 6.5. Horizontally excited tank: velocity field at $t = 314.77, 316.06$ (top row), $t = 317.34, 318.63$ (middle row), and $t = 319.91, 321.20$ (bottom row).

6.1.2 Vertical excitation

In this truly three dimensional application, we subject a rectangular tank to a periodic vertical excitation. Experimental and theoretical evidence [55, 56] indicates the existence of multiple solution branches when the horizontal cross-section of the tank is nearly square. Depending on the excitation frequency, the competing wave modes interact generating complex periodic, as well as chaotic, wave behavior. The particular case considered here is based on the experiment performed by Feng and Sethna [56]. The problem under consideration is:

- The geometry of this problem is similar to the one described in the last subsection. The dimensions of the tank are now $W = 0.1778\,\mathrm{m}$ $(7\,\mathrm{in}), H = 0.18034\,\mathrm{m}$ $(7.1\,\mathrm{in})$ and $D = 0.127\,\mathrm{m}$ $(5\,\mathrm{in})$. Boundary conditions and surface normal determination remain unchanged.

- In addition to the gravitational acceleration of magnitude $g = 9.81\mathrm{ms}^{-2}$ acting downward, the tank is subjected to a sinusoidal vertical excitation $Ag\sin\omega t$ with $\omega = 2\pi f,\ f = 4.00\,\mathrm{Hz}$ and A such that the amplitude of the oscillations remains at $1\,\mathrm{mm}$.

- At each time level, the domain is discretized using 7,066 nodes and 6,000 brick trilinear elements. The space-time mesh for each time slab consists of 14,112 nodes and 6,000 quadrilinear four-dimensional brick elements.

- As it is done in the previous case, the problem is non-dimensionalized. Dimensional scales are chosen so that the x-dimension length and vertical acceleration become unity. Table 6.2 summarizes the parameters used in this problem.

- As in previous case, a GMRES solver with diagonal scaling was used. Krylov space size was 40 was chosen, and maximum number of outer GMRES iterations was 5 initially, and 10 for larger fluid motions. At each time step, an average of 3 non-linear iterations were needed. The simulations were done in 64-bit precision on the CM-200 computer.

	Dimensional	Non-dimensional
Lengths	$D = 0.127\,\mathrm{m}$	$\tilde{D} = 0.714$
	$H = 0.18034\,\mathrm{m}$	$\tilde{H} = 1.0143$
	$W = 0.1778\,\mathrm{m}$	$\tilde{W} = 1.0$
Frequency	$f = 4.00\mathrm{s}^{-1}$	$\tilde{f} = 0.5386$
Acceleration	$g = 9.81\mathrm{ms}^{-2}$	$\tilde{g} = 1.0$
Viscosity	$\nu = 1.0 \times 10^{-6}\mathrm{m}^2\mathrm{s}^{-1}$	$\tilde{\nu} = 4.259 \times 10^{-6}$
Time step	$\Delta t = 0.0125\mathrm{s}$	$\Delta\tilde{t} = 0.093$

Table 6.2. Vertically excited tank: parameters.

The computations start with a perturbed solution which has been obtained by running the simulation for 20 time steps (one excitation period), with an additional force components applied in the x and y directions. These components have the same amplitude and frequency as the vertical one. At the end of the perturbation period, the surface of the fluid becomes deflected by about 7% from the original flat position. The additional forces are removed, and motion of the fluid continues influenced by the vertical excitation only. Figures 6.6–6.9 show the time histories of the wave height at the four corners of the container. To get a better idea of how much of the wave motion is contributed by the two competing modes (1,0) and (0,1), we also show the wave height reading at points $(x, y) = (W, H/2)$ and $(x, y) = (W/2, H)$. These points correspond to the location of probes in the experiment of Feng et al. [56], and are referred to as A1 and A2 respectively. The A1 amplitude identifies the (1,0)-mode component and amplitude at A2 indicates the strength of the (0,1)-mode. The time histories of these two amplitudes are shown in Figures 6.10 and 6.11. Even though the perturbation exhibited no preference for either of the two modes, after its removal we witness the growth of the (0,1)-mode.

Figures 6.12–6.14 show, for one period of oscillations, the perspective view of the water surface and surface contours. The elevation plots are viewed from the negative x direction. In the z direction, the visible bounding box extends from 0.5 to 0.9. These snapshots are taken in the initial phase after the removal of the perturbation,

when a mixed mode with nearly equal (1,0) and (0,1)-mode components is evident.

Another period of the wave motion is shown in Figures 6.15–6.17. Here the (0,1)-mode is dominant, with a small, but non-zero, (1,0)-mode component. The two competing modes have a slight phase difference, leading to a small "rotating" effect. Such phase difference can be also ascertained by comparing Figures 6.10 and 6.11. The experimental data predicts the presence of a mixed mode (called MS1 in [56]) at this frequency. The experimental amplitude of the (0,1)-mode is 0.15, which compares well with the numerical result (0.14 and growing slightly). The amplitude of the (1,0)-mode obtained in the simulation is seen as 0.04 and falling, which is lower than the experimental value of 0.08.

The common experience with the two sloshing problems presented in this section is the presence of long-lasting transients which make reaching the final quasi-steady state quite costly. Unfortunately this may be expected in all simulations involving fluids of low viscosity.

Performance tests were conducted for the space-time implementation, with the sloshing problem serving as a benchmark, yielding following results. On the 32K processor CM-200 computer, the formation of the element level matrices and residuals took place at 800 million 64-bit floating point operations per second (megaflops). The GMRES solution phase speed was observed as 872 megaflops. For a three dimensional space-time formulation, the bulk of time taken by the GMRES solution process is consumed by the matrix vector product (see Box 5.3). As discussed in Section 5.3, this product involves three components: gather, on-processor matrix vector multiplication and scatter. Only the second component contributes to the floating point operation count. The ratio of the computation time consumed by the three stages was found to be 2:1:2. Thus the 872 megaflops speed for the entire GMRES solver indicates that the on-processor matrix vector product is being computed near its peak speed of 5 gigaflops. The performance of the entire code, including the parallel input/output operations and problem setup, was 794 megaflops. As the speeds of the two major code parts, i.e. the matrix formation stage and the GMRES solution stage, are comparable, the overall performance of the program should not be sensitive

to the choice of parameters such as the number of outer or non-linear iterations. Nevertheless, such sensitivity may exist in other situations, as indicated by the timings for the two-dimensional problems presented in the following section.

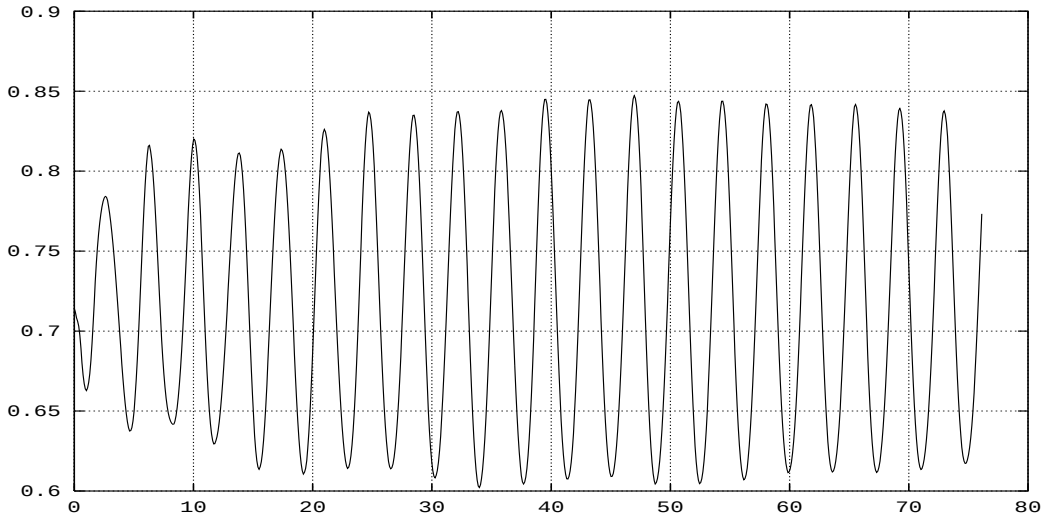

Figure 6.6. Vertically excited tank: time history of the wave height at the $(x, y) = (0, 0)$ corner.

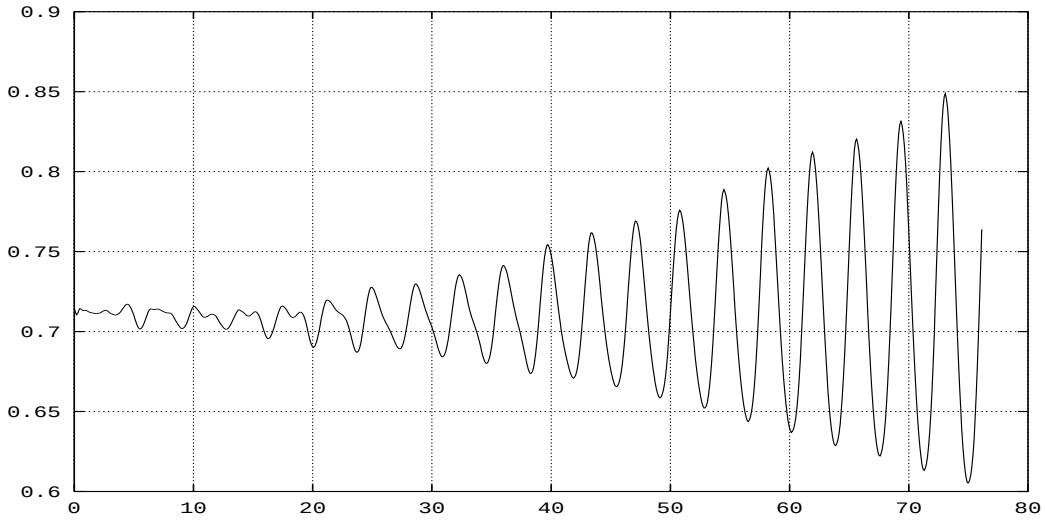

Figure 6.7. Vertically excited tank: time history of the wave height at the $(x, y) = (W, 0)$ corner.

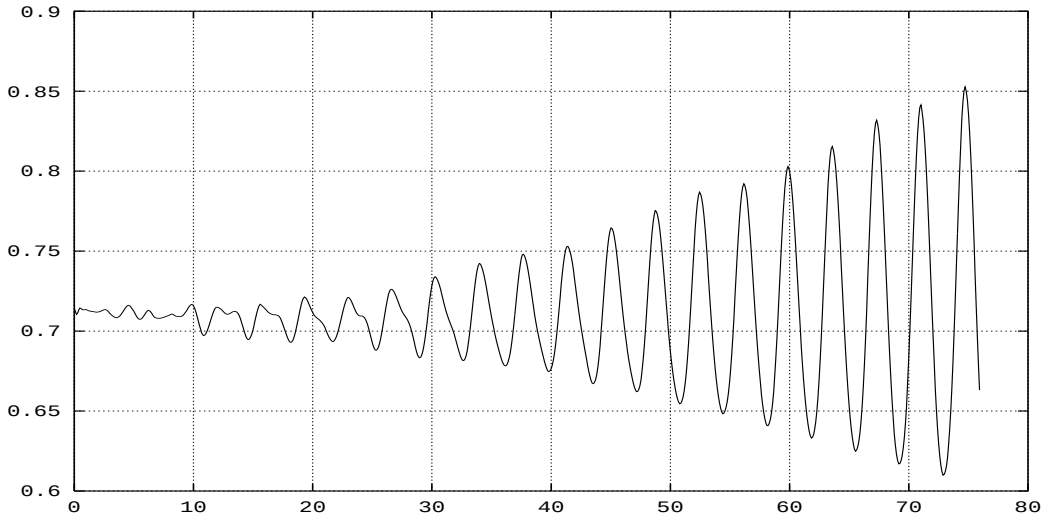

Figure 6.8. Vertically excited tank: time history of the wave height at the $(x, y) = (0, H)$ corner.

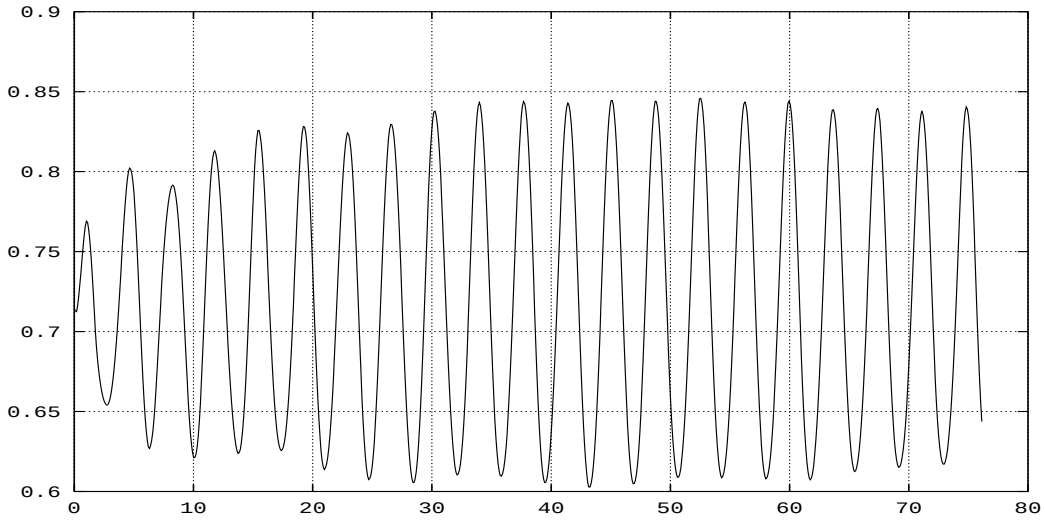

Figure 6.9. Vertically excited tank: time history of the wave height at the $(x, y) = (W, H)$ corner.

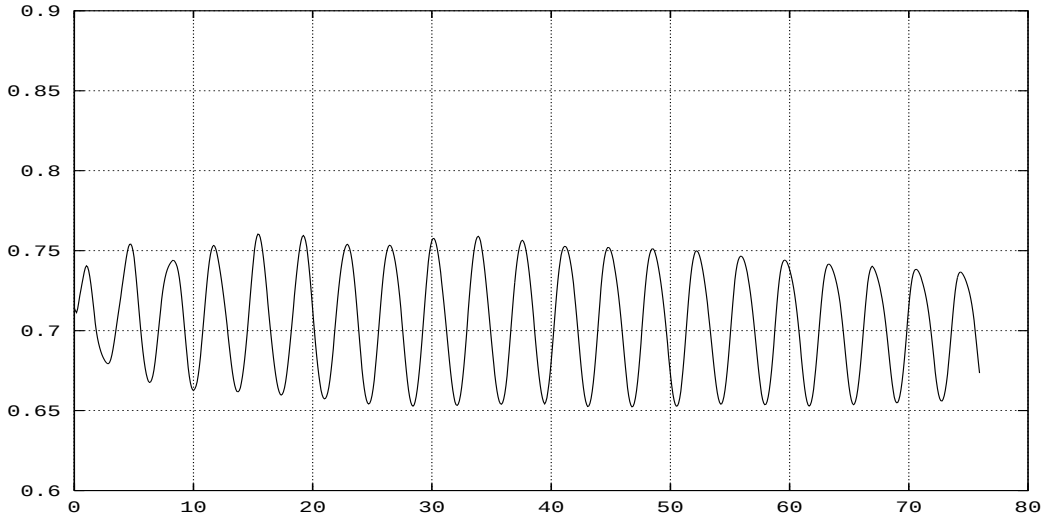

Figure 6.10. Vertically excited tank: time history of the wave height at point A1.

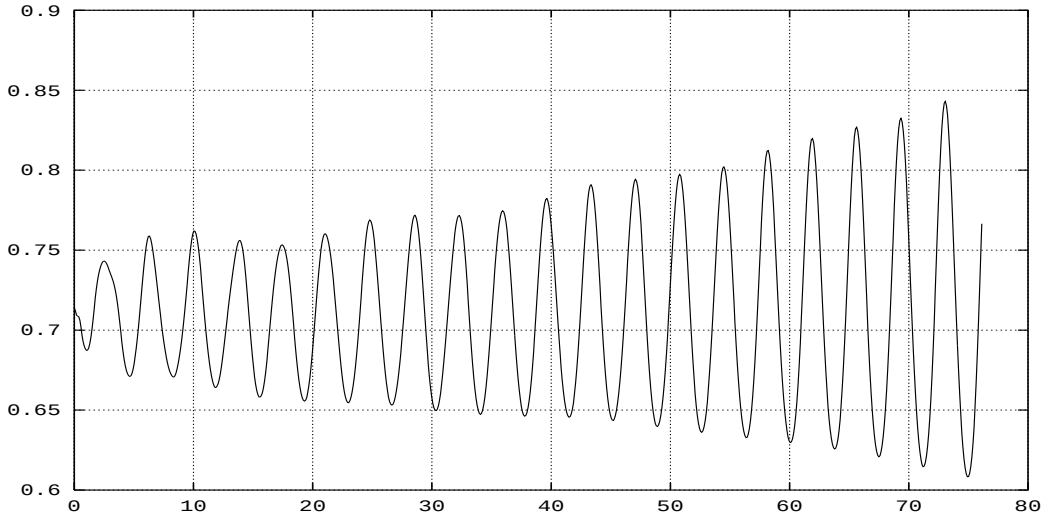

Figure 6.11. Vertically excited tank: time history of the wave height at point A2.

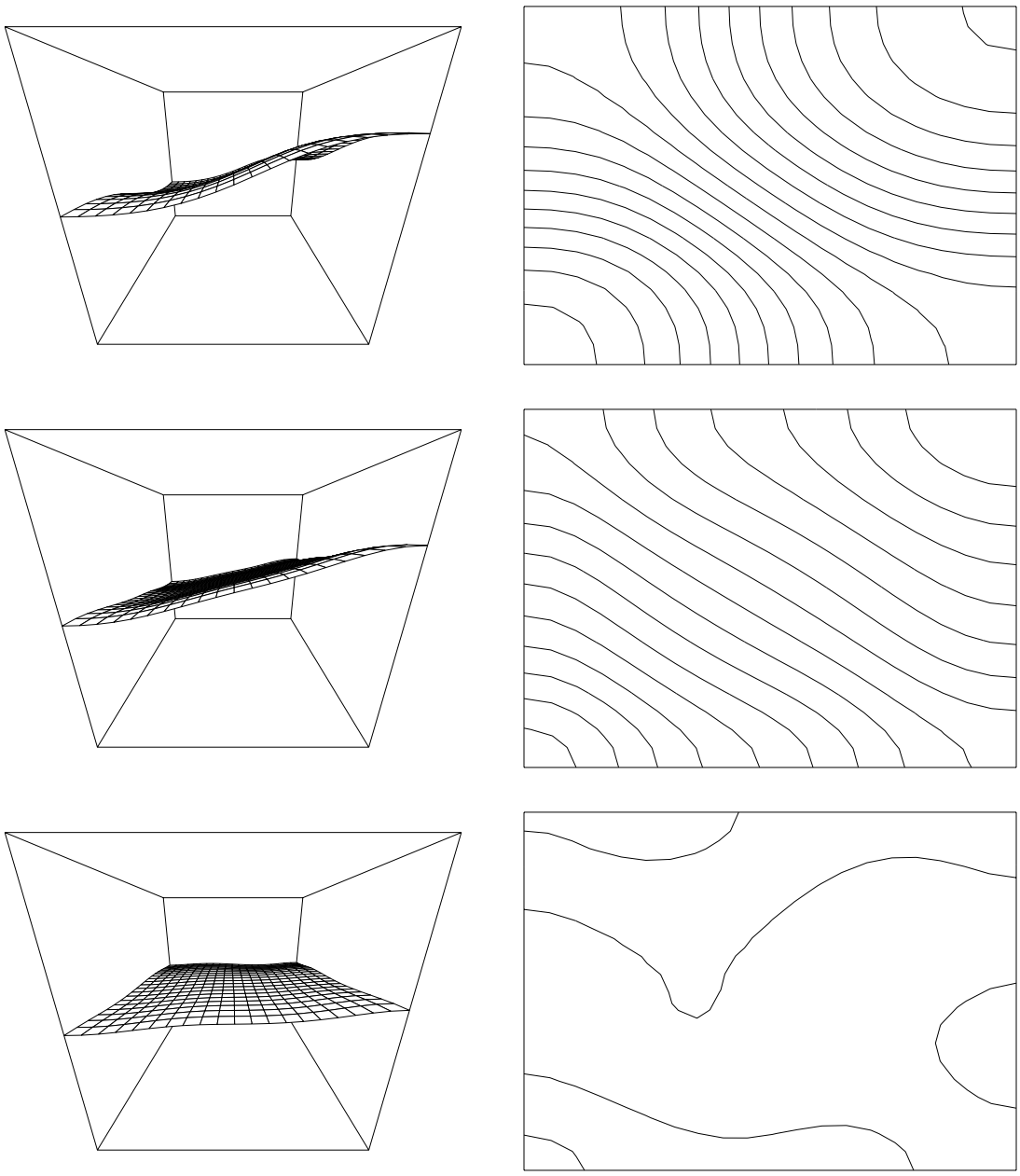

Figure 6.12. Vertically excited tank: free surface view and isolines at $t = 13.74$, 14.20, and 14.67 (from top to bottom).

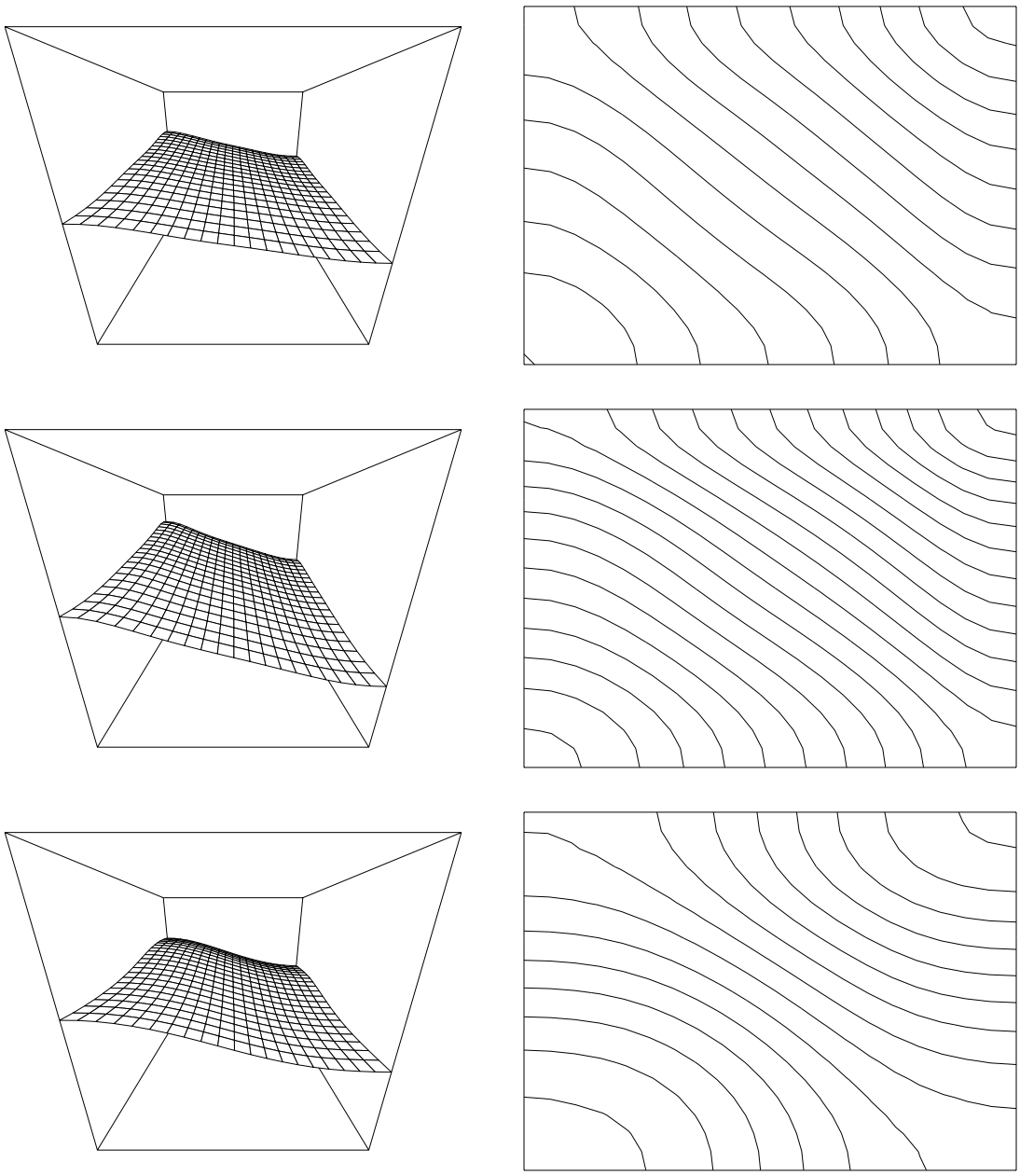

Figure 6.13. Vertically excited tank: free surface view and isolines at $t = 15.13$, 15.60, and 16.06 (from top to bottom).

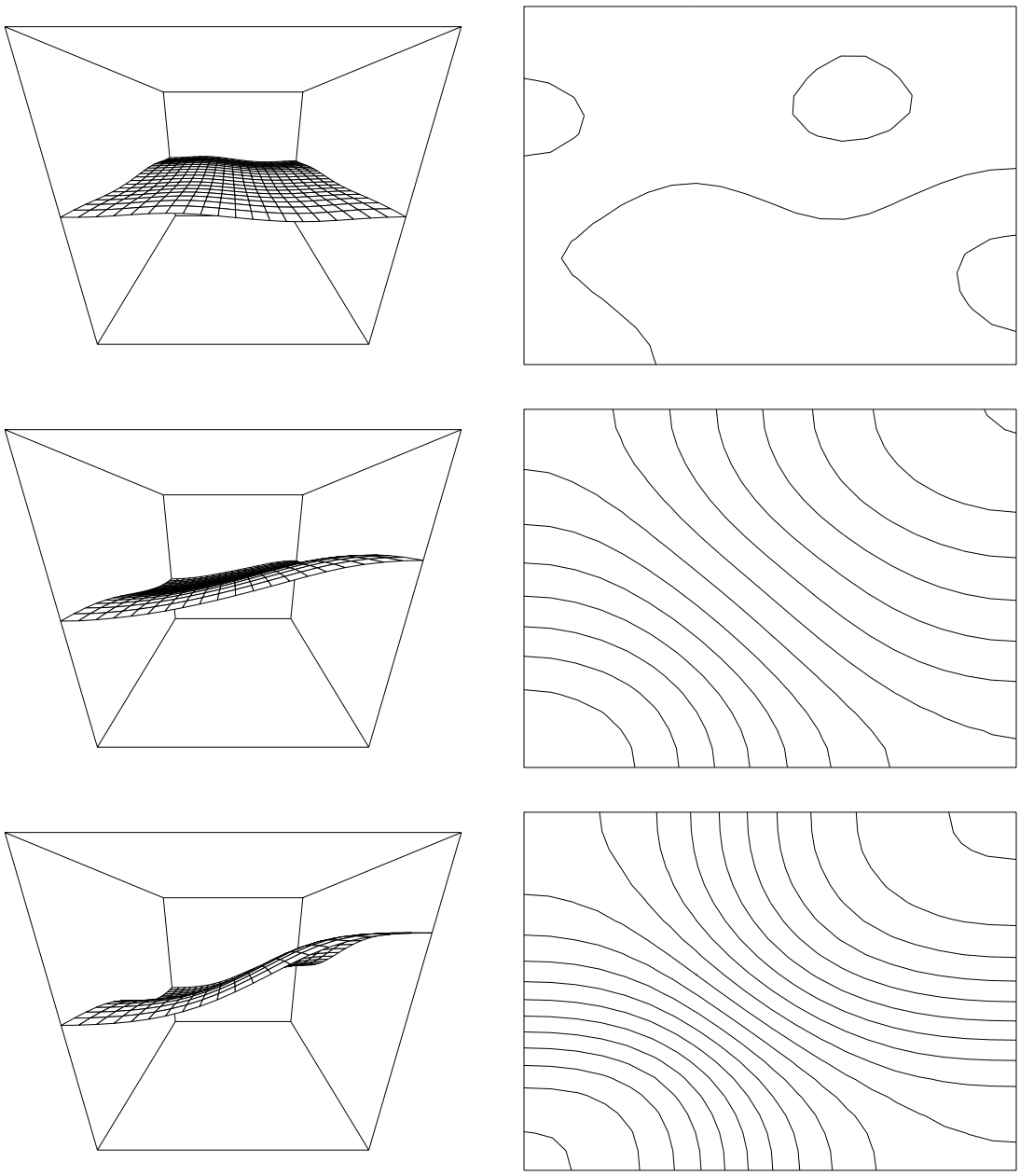

Figure 6.14. Vertically excited tank: free surface view and isolines at $t = 16.52$, 16.99, and 17.45 (from top to bottom).

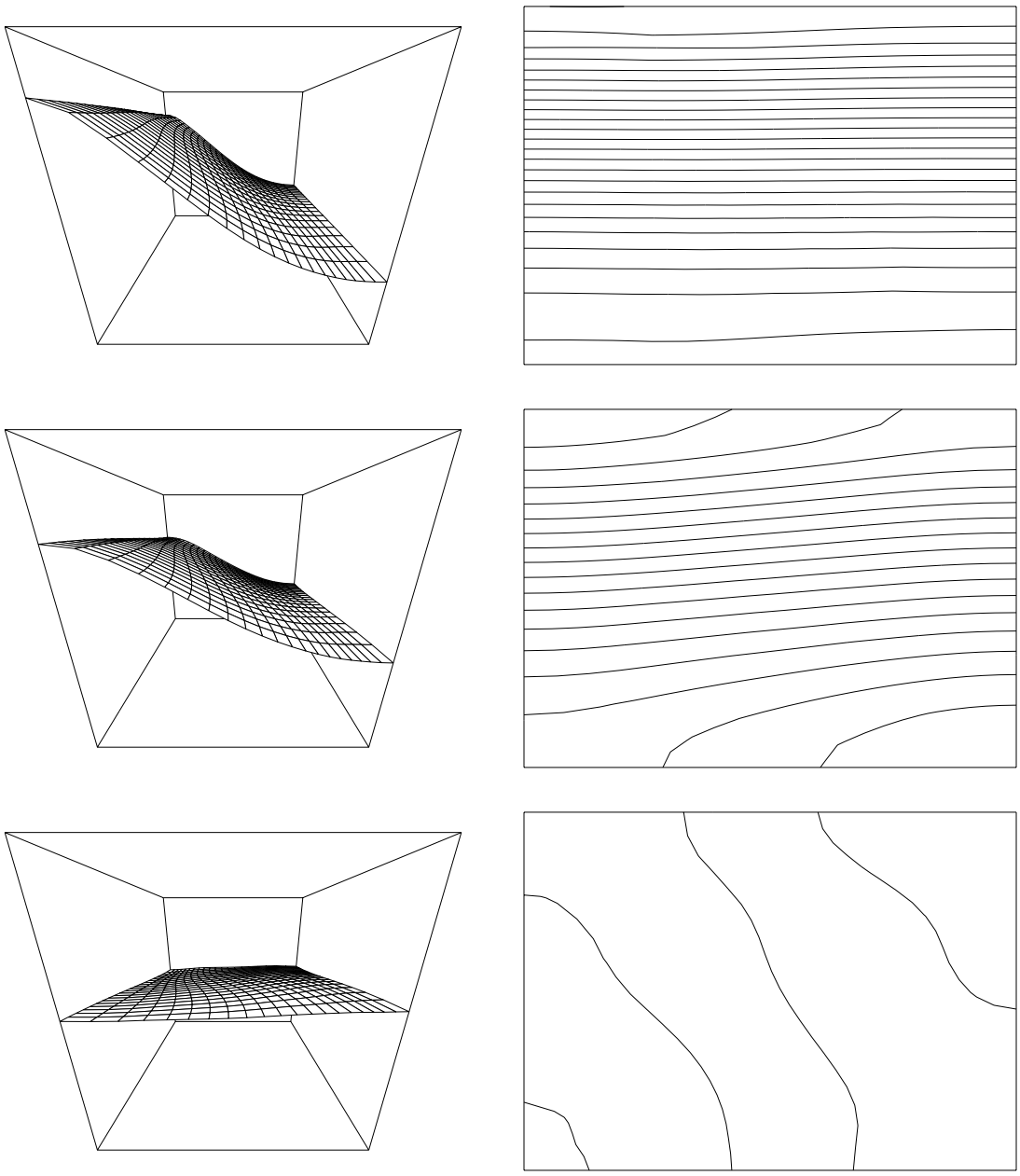

Figure 6.15. Vertically excited tank: free surface view and isolines at $t = 71.29$, 71.76, and 72.22 (from top to bottom).

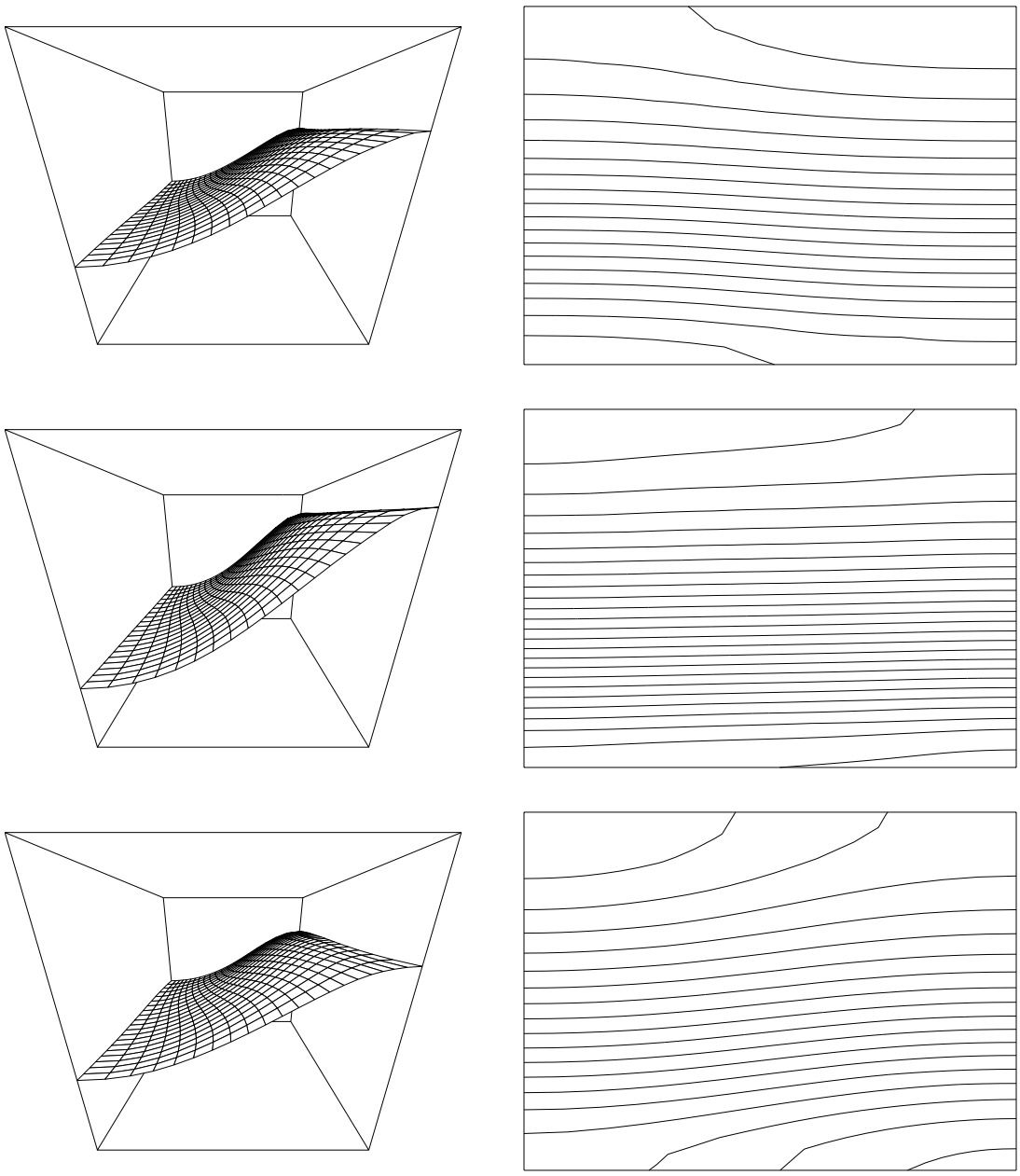

Figure 6.16. Vertically excited tank: free surface view and isolines at $t = 72.69$, 73.15, and 73.61 (from top to bottom).

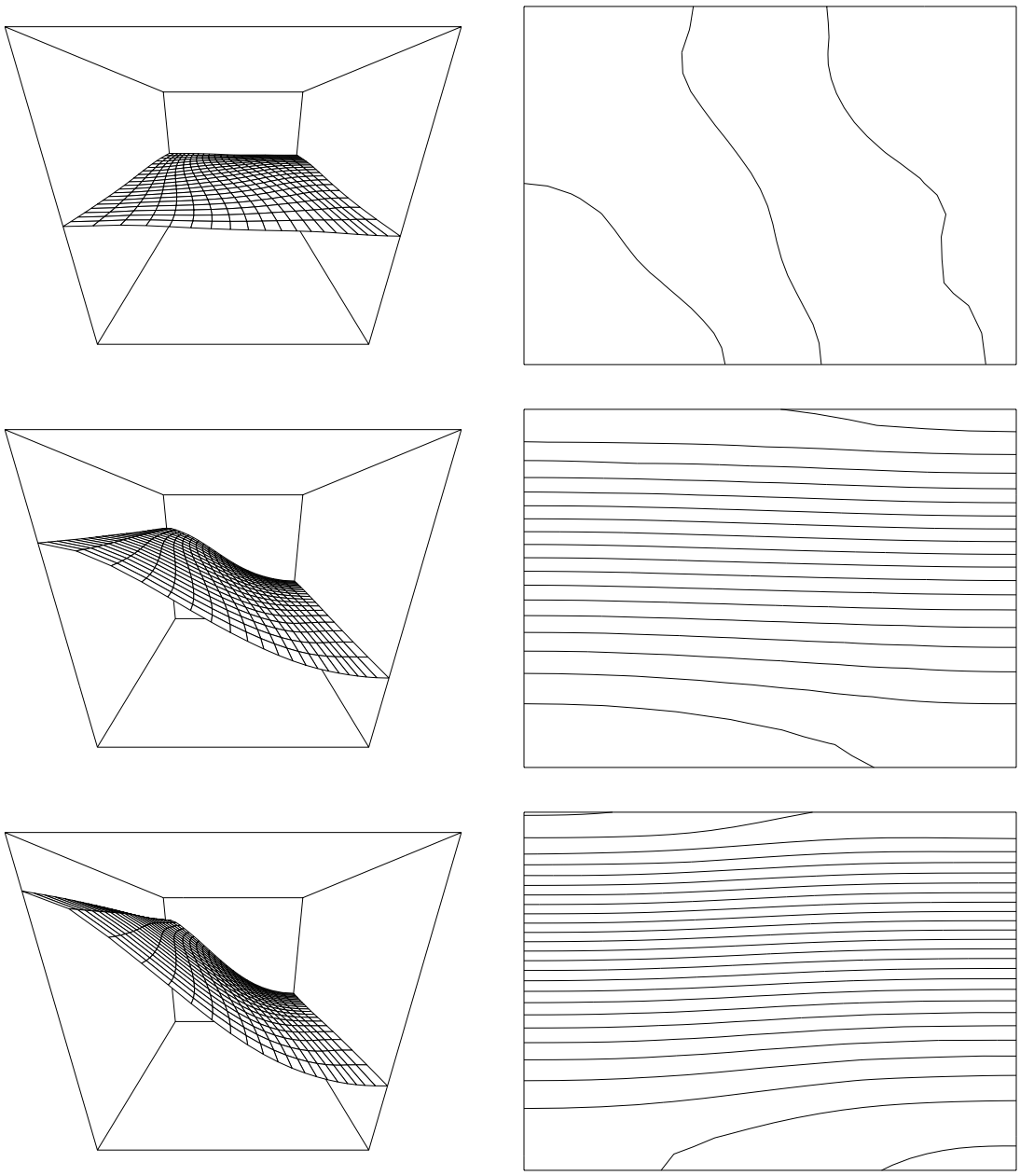

Figure 6.17. Vertically excited tank: free surface view and isolines at $t = 74.08$, 74.54, and 75.00 (from top to bottom).

6.2 Flows Past a Circular Cylinder

Flow past a circular cylinder has become a traditional benchmark problem used to test the performance of various numerical methods. Contributing to its popularity is the well-known behavior at low Reynolds numbers, repeatedly seen in experiments [57] and past computations [58–60]. At the same time, at Reynolds numbers above 40 the problem possesses non-trivial time-dependent solutions. The famous von Karman vortex street can challenge the time-stepping properties of the numerical scheme. The changes in flow characteristics observed as the Reynolds number increases are also relevant from the point of view of dynamical system analysis. In this section, the basic stress-velocity-pressure formulation is used to simulate two-dimensional flow past a cylinder at Reynolds numbers ranging from 1,000 to 10,000. The problem is formulated as follows:

- A circular cylinder of unit radius is enclosed in a rectangular domain, as shown in Figure 6.18. At the inflow boundary Γ_{in} we specify a unit horizontal velocity component U, the upper and lower boundaries Γ_{upper} and Γ_{lower} are taken as flow symmetry lines, and traction-free boundary condition is imposed at the outflow boundary Γ_{out}. The cylinder surface $\Gamma_{cylinder}$ is assumed to be a no-slip boundary. The upstream and horizontal boundaries are located 16 units each from the cylinder center, while the downstream boundary is 45 units away.

- A semi-structured mesh with 21,747 nodes and 21,408 elements covers the domain, as shown in Figure 6.19. The size of the smallest elements, i.e. the ones adjacent to the cylinder, is approximately 0.0327×0.01.

- In later computations the domain was extended to 65 units downstream from the cylinder, by adding a vortex dissipation zone with purposefully coarse elements. This remedy was necessitated by several occurrences of the inflow at the downstream boundary. Especially the strong startup vortices, when advected downstream, would occasionally interact with each other to provide a small region of negative x-component of velocity at the outflow, making the

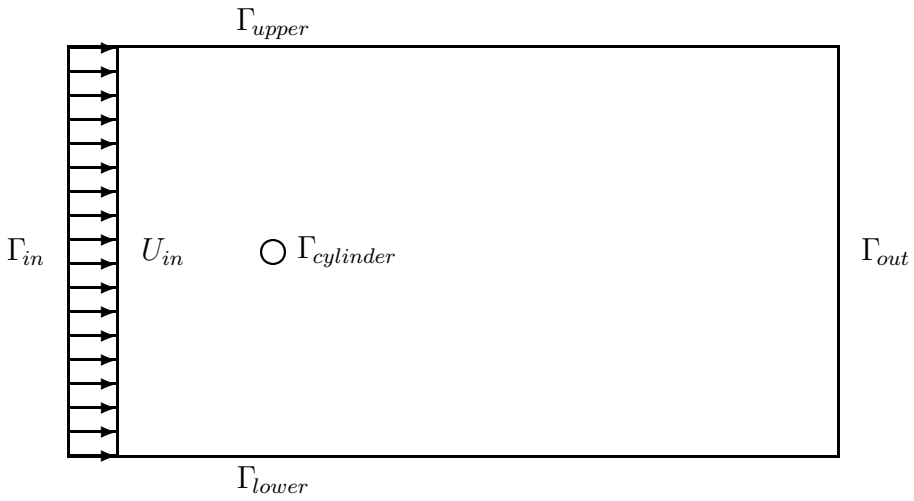

Figure 6.18. Flow past a circular cylinder: domain description.

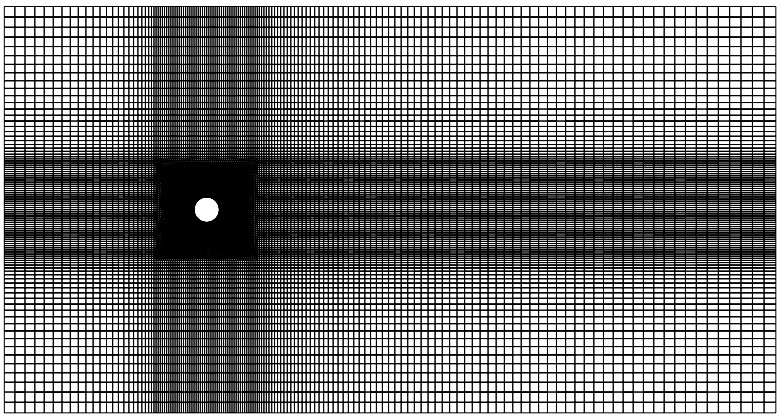

Figure 6.19. Flow past a circular cylinder: finite element mesh.

problem ill-posed at the subsequent time steps. In such cases, the artificially coarse mesh added downstream provided the necessary dissipation of the vortices, without disturbing the solution upstream. The extended mesh with 22,299 nodes and 21,968 elements is shown in Figure 6.20. It was used to compute the flows at $Re = 2,000$ and $Re = 4,000$. Finally, the accuracy of the solution at $Re = 1,000$ was confirmed by interpolating the time dependent solution to a new mesh (not shown here) with 50,827 nodes and 50,320 elements. This mesh

was characterized by twice the resolution of the original mesh in both radial and tangential directions around the cylinder. The simulation was continued with the refined mesh, and the time trace of the aerodynamic coefficients observed. After initial shake-up due to the pressure changes downstream (the extended downstream region of the refined mesh has been assigned uniform flow conditions, as the original mesh did not extend that far), the drag and lift oscillations settled to within 1% of their original amplitudes and means. That led us to believe that the two original meshes shown in Figures 6.19 and 6.20 provide sufficient resolution, at least for Reynolds numbers close to $Re = 1,000$.

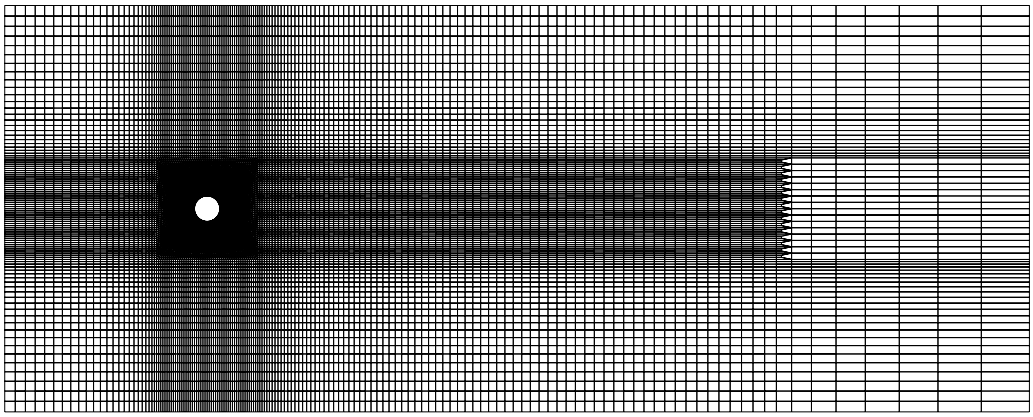

Figure 6.20. Flow past a circular cylinder: extended finite element mesh.

- Based on the expected value of the Strouhal number ($St = D/UT = 0.2$, where D is the diameter and T is the vortex shedding period), the time step size in most cases is selected as $\Delta t = 0.1$, to provide good temporal resolution, i.e. roughly 100 time steps per period.

- All the cases discussed below share the use of a GMRES solver with diagonal scaling. The computations were performed in 64-bit precision on the CM-200 computer, with the exception of the Reynolds number 1,000 case, which was calculated on the CM-5 machine.

6.2.1 Reynolds number 1,000

At the lower end of the studied spectrum we obtain a familiar vortex street — periodic and regular. Apart from the minor changes in the vortex pattern, this solution resembles the periodic solutions at Reynolds number 100, seen often in the numerical tests. In fact, we have no reason to suppose that anything extraordinary occurs inside the entire $40 < Re < 1000$ range.

The initial condition for the simulation is the steady-state solution at Reynolds number 100. The viscosity is decreased tenfold, and the time-dependent terms in the formulation are enabled. A time step size of 0.05 was selected to provide sufficient resolution of the vortex shedding periods, which are expected to be of the order of 10. Later experience indicated that such temporal resolution was unnecessary for the range of Reynolds number discussed here, and for subsequent simulations the time step was increased to 0.1.

In the solution phase, the GMRES solver with the Krylov subspace dimension of 20 was used. The number of outer GMRES iterations was set to 5, and the method took at most 4 nonlinear iterations to converge at each time step. At the end of each Newton iteration loop, the initial residual was reduced by 5 orders of magnitude, and its norm was below 10^{-6}.

Figure 6.21 shows the vorticity fields at several instants leading to the establishment of the periodic vortex shedding, starting with the symmetric initial condition. Figure 6.22 shows in detail the flow field during one period of the vortex shedding. The four frames correspond to, from top to bottom, the zero, maximum, zero and minimum values of the lift coefficient. A magnified view around the cylinder is also provided in the left column. Figures 6.23 and 6.24 show the time histories of the drag and lift coefficients. The Strouhal number, St, is computed to be 0.241. The drag coefficient varies from a minimum of 1.298 to a maximum of 1.756. The lift coefficient oscillates between -1.45 and $+1.45$. These values are very close to the values obtained in separate experiments for $Re = 950$, using velocity-pressure space-time formulation. They differ however from the experimental data of $St = 0.21$ and mean

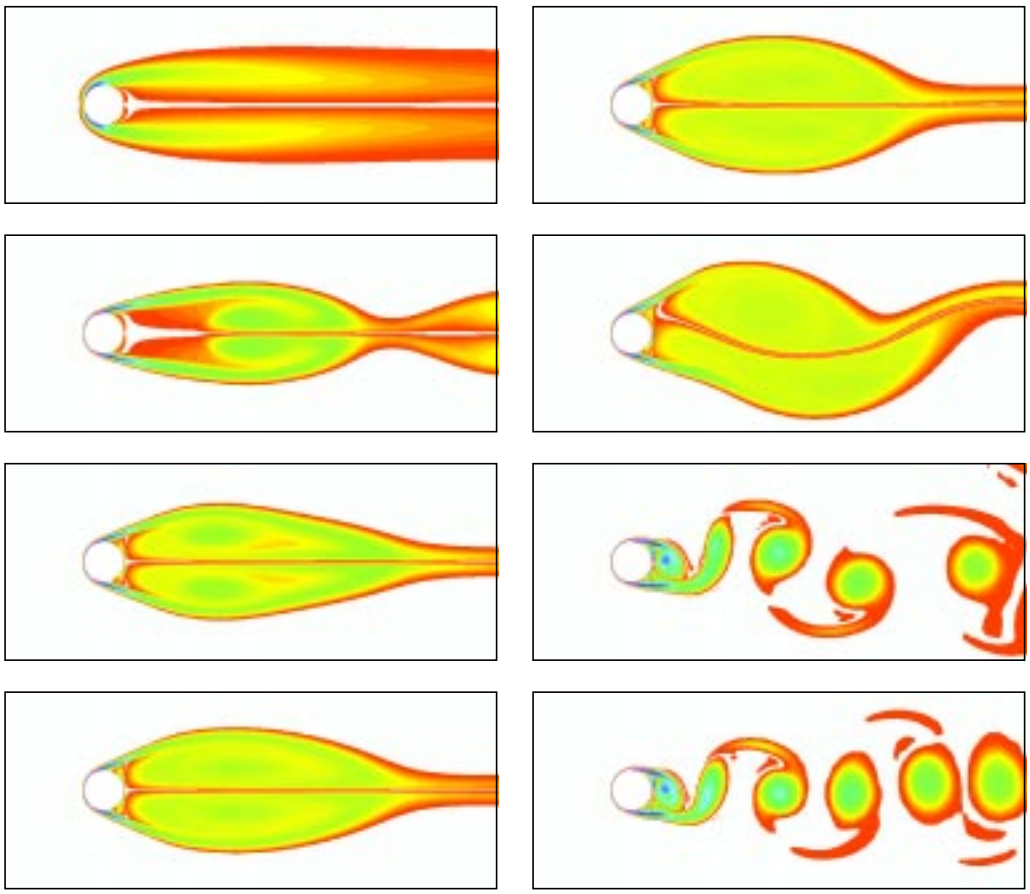

Figure 6.21. Flow past a circular cylinder at Reynolds number 1,000: vorticity field at $t = 0$, 25, 50, 75, 100, 125, 150 and 175.

drag coefficient of 1.2 as quoted in [57]. Higher than expected values of the drag coefficient were also recently reported by Tabata [60]. This discrepancy may be due to the two-dimensional character of the numerical simulations. It can be expected that at these Reynolds numbers, three-dimensional and turbulence effects begin to significantly influence the aerodynamic forces acting on the body. This is in contrast with the standard $Re = 100$ case, where the agreement between the numerical solution and the laboratory experiment is satisfactory.

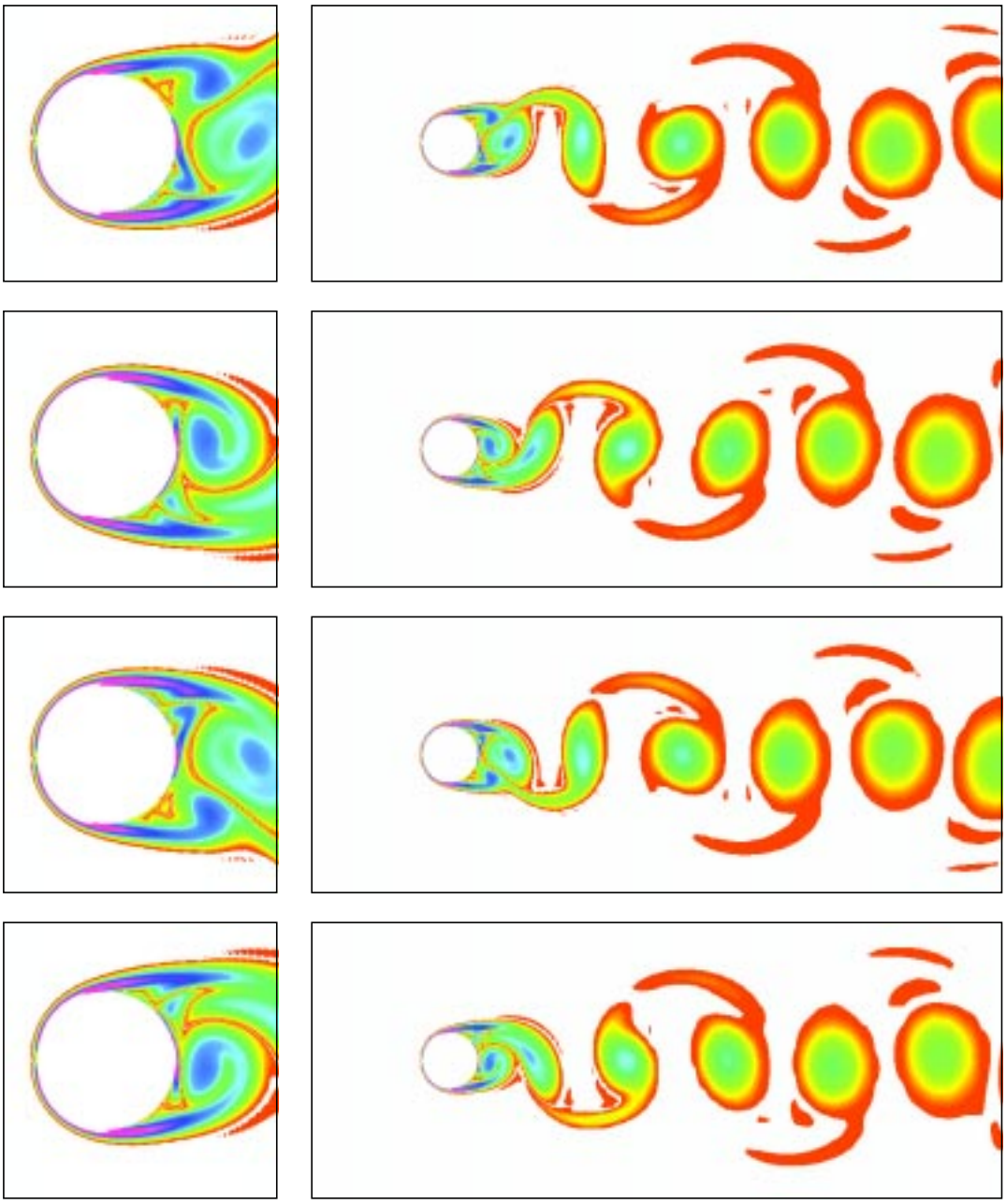

Figure 6.22. Flow past a circular cylinder at Reynolds number 1,000: vorticity field at $t = 221.7$, 223.6, 225.9, and 227.7.

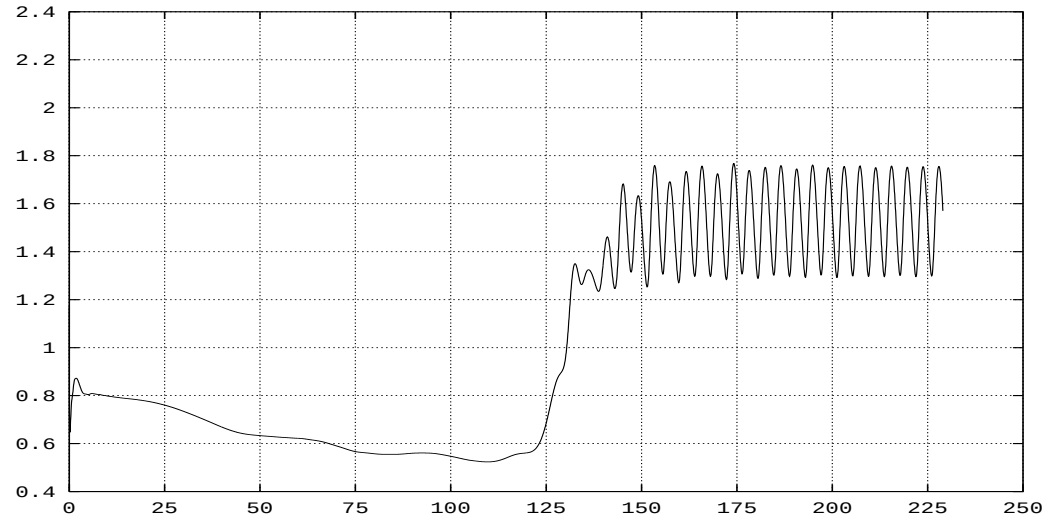

Figure 6.23. Flow past a circular cylinder at Reynolds number 1,000: time history of the drag coefficient.

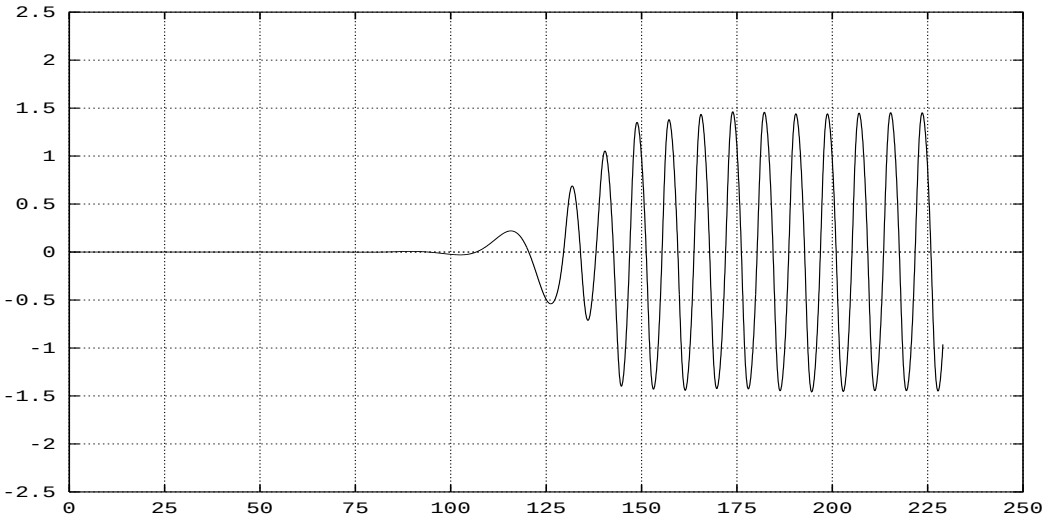

Figure 6.24. Flow past a circular cylinder at Reynolds number 1,000: time history of the lift coefficient.

6.2.2 Reynolds number 2,000

Increasing the Reynolds number to 2,000 results in a flow field qualitatively different from the previous case. Again the steady flow at Reynolds number 100 serves as an initial condition. The evolution of the flow is shown in Figures 6.25 and 6.26. Due to the complex temporal behavior of the flow at this and higher Reynolds numbers, this and later flow evolution figures show more frequent snapshots of the flow field than for Reynolds number 1,000. For $0 < t < 90$ the flow retains its symmetric character. At $t \approx 100$ the small asymmetric perturbances caused by the machine round-off errors accumulate sufficient strength to cause a global loss of symmetry. After the two large stationary vortices which developed in the symmetric phase float downfield, vortex shedding is established. In contrast to the stationary vortex street at Reynolds number 1,000, in the current case the vortex street oscillates about the centerline of the domain. This phenomenon is also evident in the drag and lift coefficient plots, in which the basic vortex shedding frequency is modulated with a ~ 10 times lower secondary frequency. This is seen in Figures 6.27 and 6.28. The Strouhal number based on the primary frequency of the lift coefficient oscillations is 0.244. The GMRES solver with the Krylov subspace dimension of 40 was employed. Number of outer GMRES iterations was set to 10, and the computations required at most 3 nonlinear iterations to converge at each time step.

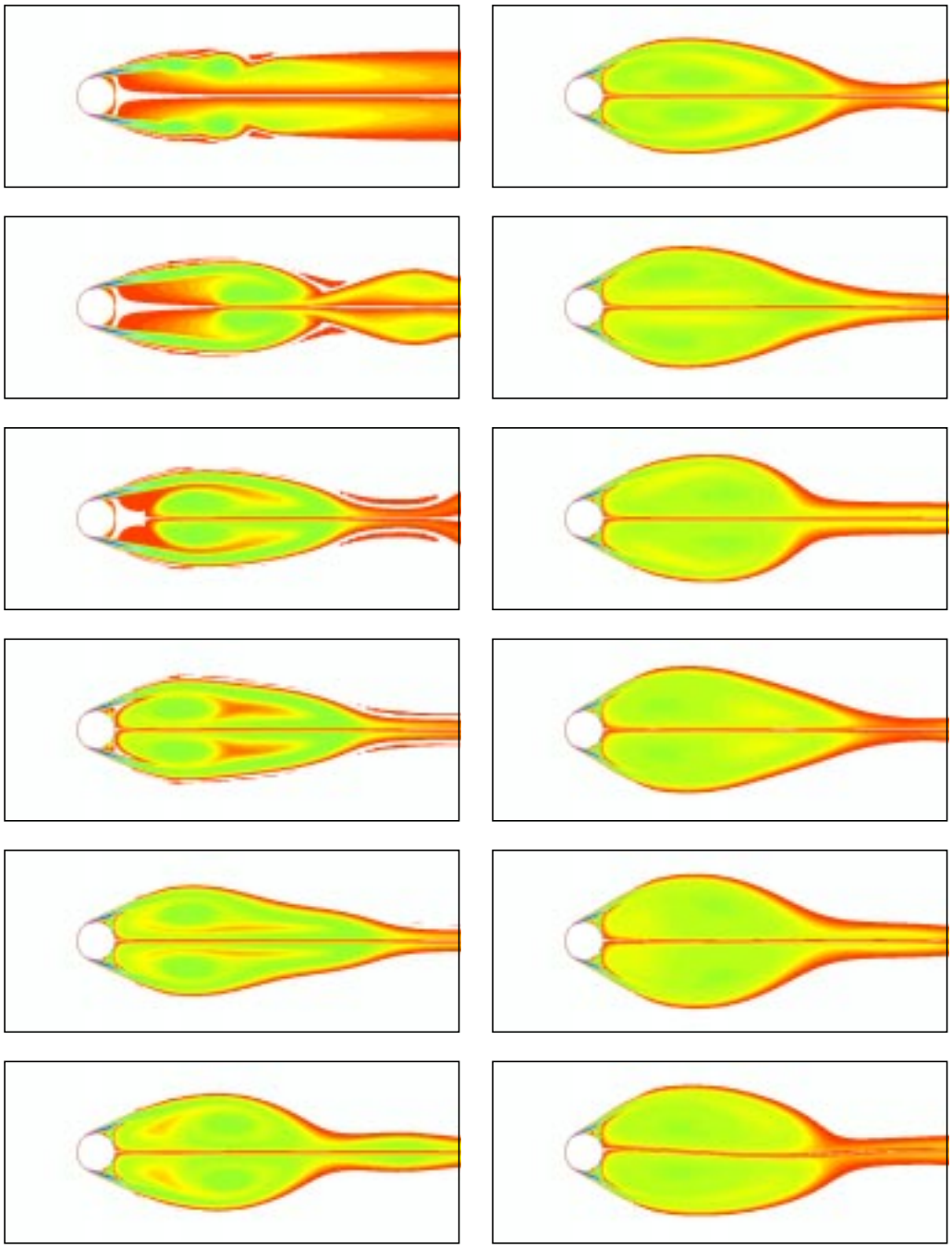

Figure 6.25. Flow past a circular cylinder at Reynolds number 2,000: vorticity field at $t = 10$, 20, 30, 40, 50, 60 (left column), 70, 80, 90, 100, 110, and 120 (right column).

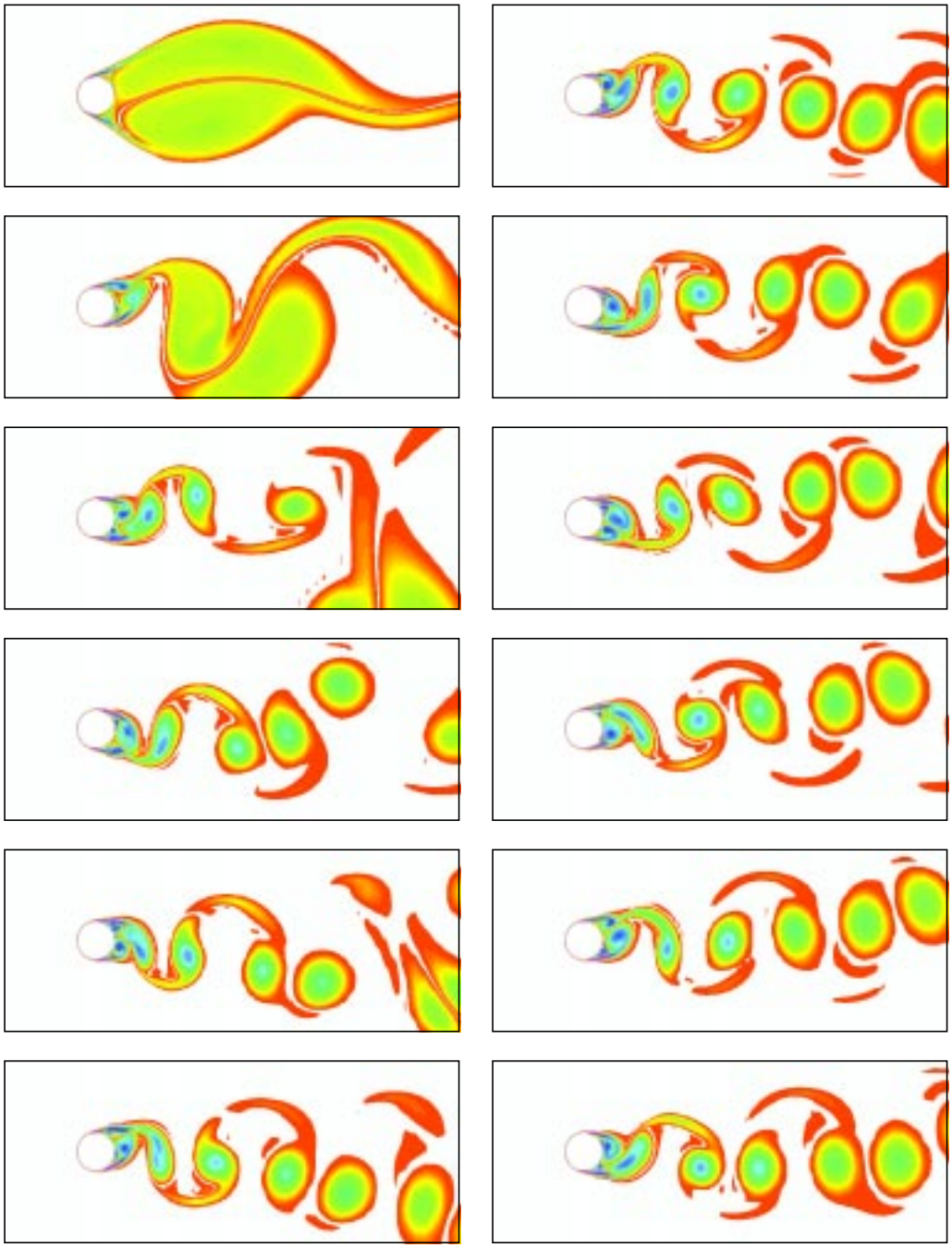

Figure 6.26. Flow past a circular cylinder at Reynolds number 2,000: vorticity field at $t = 130$, 140, 150, 160, 170, 180 (left column), 190, 200, 210, 220, 230, and 240 (right column).

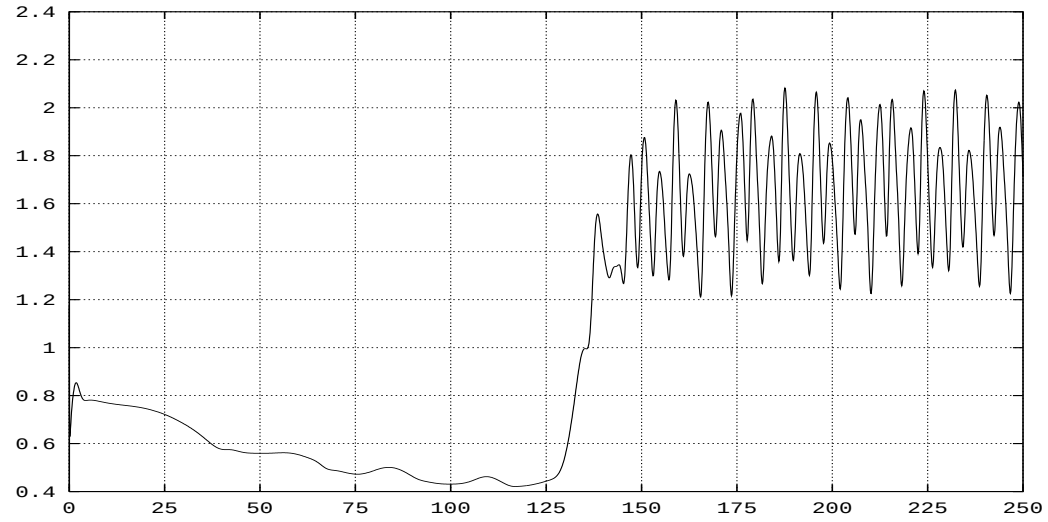

Figure 6.27. Flow past a circular cylinder at Reynolds number 2,000: time history of the drag coefficient.

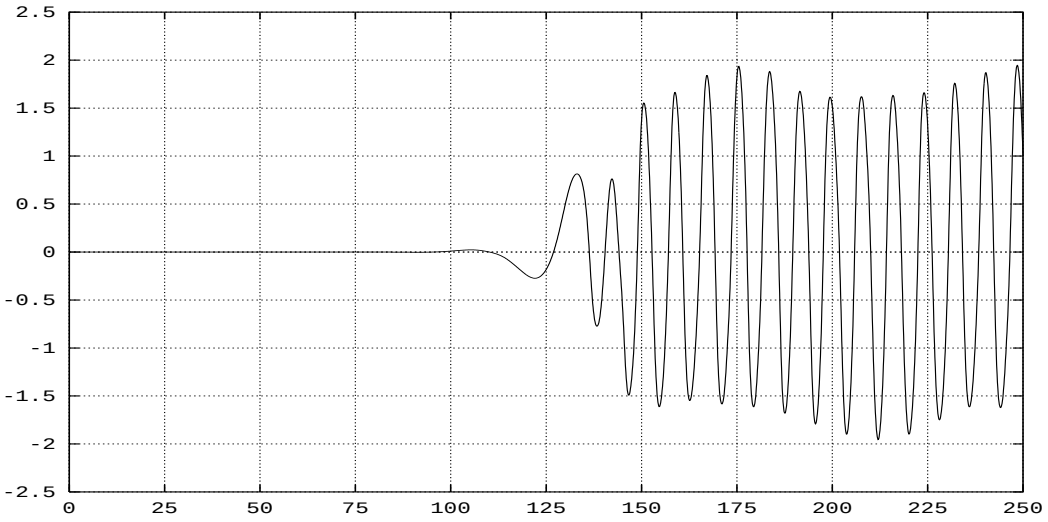

Figure 6.28. Flow past a circular cylinder at Reynolds number 2,000: time history of the lift coefficient.

6.2.3 Reynolds number 4,000

This case also starts from the steady solution at Reynolds number 100. Suspecting the importance of hysteresis effects in the studied dynamical system, it was desirable to compute as many cases as possible from the same initial condition. The evolution of the vortex street is shown in Figure 6.29, and its periodic regime is documented in Figure 6.30. Unlike previous cases, the vortex street is steadily deflected downward from the plane of symmetry of the domain. This is also evident from the non-zero mean value of the lift coefficient and non-sine-wave form of the drag coefficient oscillations, seen in Figures 6.31 and 6.32. This asymmetry was also detected in the $Re = 5,000$ case, not quoted here due to its similarity to the presently discussed simulation. When the phenomenon was first encountered at $Re = 5,000$, we proceeded to convince ourselves that the non-symmetric behavior is not due to an error in problem specification. The entire solution field was flipped about the centerline of the domain, and used as an initial condition. Indeed the flow field continued unperturbed, this time with the opposite deflection of the wake, proving that two distinct solutions are admissible by the system.

The observed Strouhal number is 0.253. The GMRES solver characteristics were the same as in the $Re = 2,000$ case.

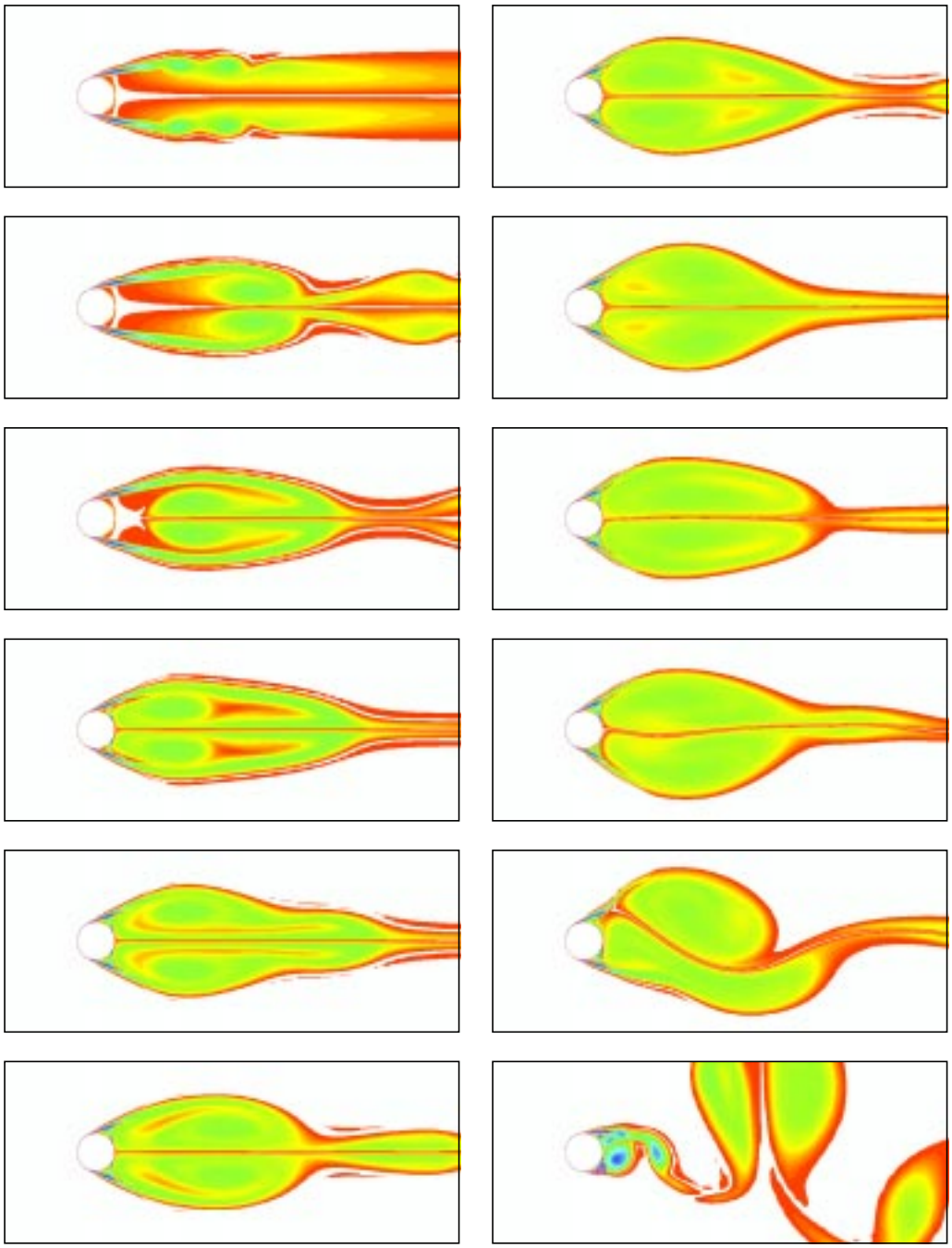

Figure 6.29. Flow past a circular cylinder at Reynolds number 4,000: vorticity field at $t = 10$, 20, 30, 40, 50, 60 (left column), 70, 80, 90, 100, 110, and 120 (right column).

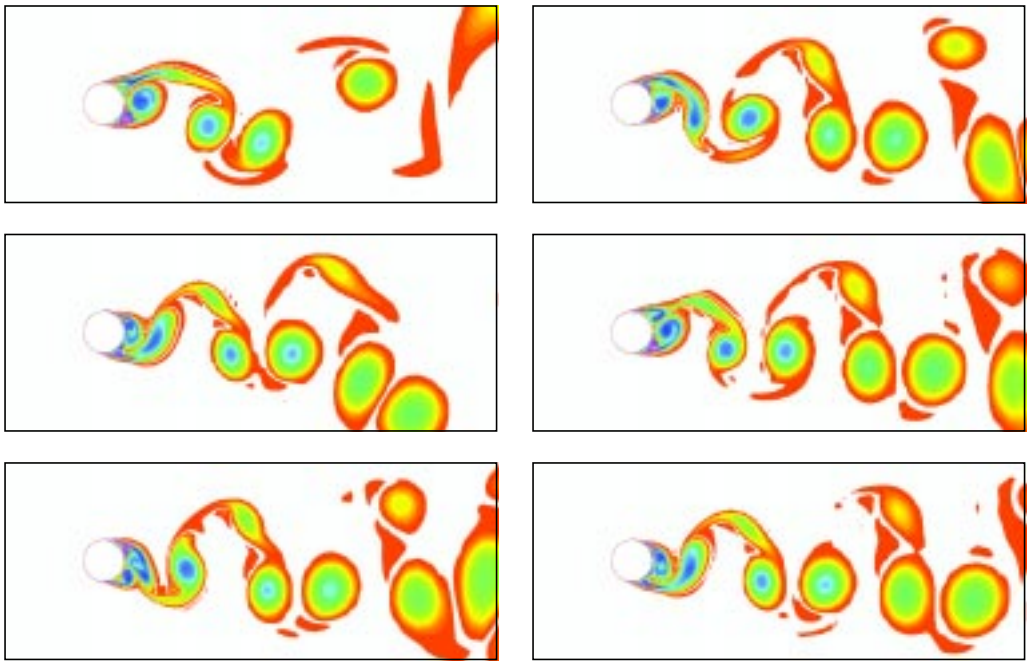

Figure 6.30. Flow past a circular cylinder at Reynolds number 4,000: vorticity field at $t = 130$, 140, 150 (left column), 160, 170 and 180 (right column).

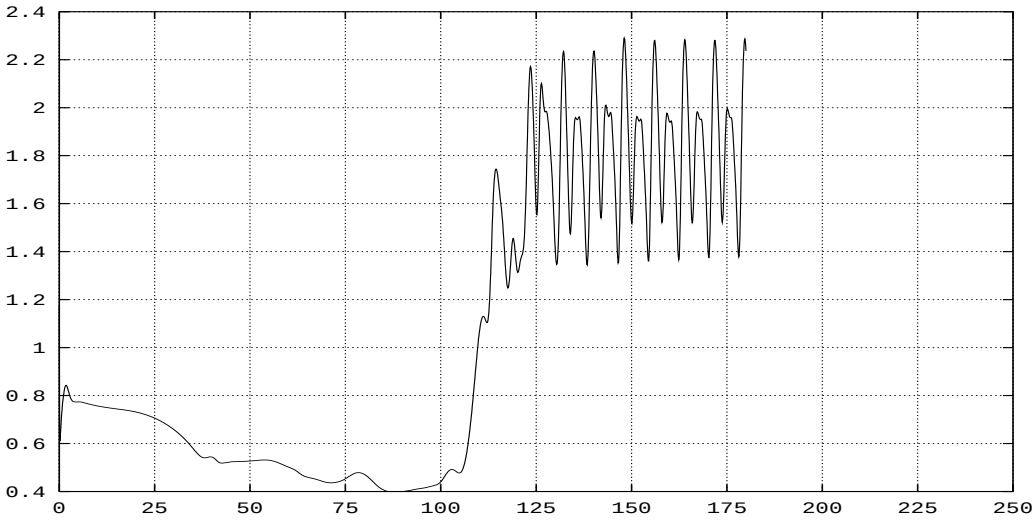

Figure 6.31. Flow past a circular cylinder at Reynolds number 4,000: time history of the drag coefficient.

6.2.4 Reynolds number 10,000

The last simulation involves flow at Reynolds number 10,000. We start from an initial condition of a time periodic flow at Reynolds number 1,000. A decreased time step size of 0.05 was used.

In this case, the GMRES solver required a Krylov subspace of size 20, with 5 outer GMRES iterations, and an average of 4 nonlinear iterations per time step.

Figure 6.33 shows the vorticity fields at several equally spaced instants after irregular flow field seems fully developed. In contrast to the other cases discussed in this section, many different frequencies appear to be present in the drag and lift coefficient fluctuations, as seen in Figures 6.34 and 6.35.

It should be noted that the above simulations are relevant from the point of view of dynamical system analysis. The dynamical system in question is governed by strictly two-dimensional Navier-Stokes equations. In practical flows at this Reynolds number, the three-dimensional effects, most notably the onset of turbulence, cannot be

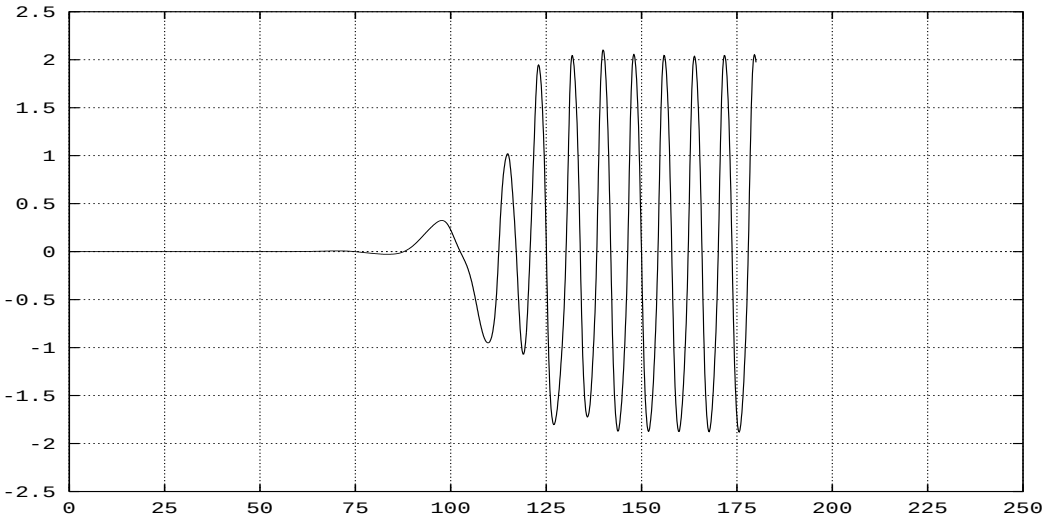

Figure 6.32. Flow past a circular cylinder at Reynolds number 4,000: time history of the lift coefficient.

ignored. Comparison with experimental data contained e.g. in [57] and [61] reveals that higher than expected values of mean drag coefficient, amplitude of the lift coefficient and vortex shedding frequency are obtained with the current two-dimensional simulations. The "dead water zone", prominently appearing downstream of the cylinder in visualizations contained in [61], is also absent from the two-dimensional flow.

The performance of the parallel two-dimensional velocity-pressure-stress implementation was found to be slightly different than for the three-dimensional cases mentioned earlier. Due to the smaller storage requirements for the element-level matrices, two-dimensional problems can employ higher number of elements for the same memory usage. This leads to an increase in the extents of parallel dimensions and a corresponding decrease in the serial dimensions of the variables involved in the matrix formation phase (see [21] for the explanation of concepts of serial and parallel dimensions). The result is an increase in the matrix formation speed to 1.607 gigaflops on a 32K-processor CM-200 machine. In the GMRES solution phase more time was consumed by the Gramm-Schmidt orthogonalization process (see Box 5.3).

This resulted in an overall speed decrease for the GMRES stage to 518 megaflops. Total performance including all program stages was measured at 561 megaflops, with GMRES part accounting for most of the computations, and consequently, high influence on the total speed. Note that the performance measurements improved by about 15% with respect to those quoted in [21] for an equivalent problem due to hardware improvements. The disparate timings for the GMRES and matrix formation steps may influence the choice of solver parameters. For example, with a fixed sum of outer GMRES iterations per time step, the high speed of the formation phase prompts us to compute left hand side more often, i.e., reduce the number of outer iterations in a non-linear iteration, but increase the number of non-linear iterations per time step. The small price paid in the more frequent left hand side recalculations often will pay off in the faster convergence within a time step.

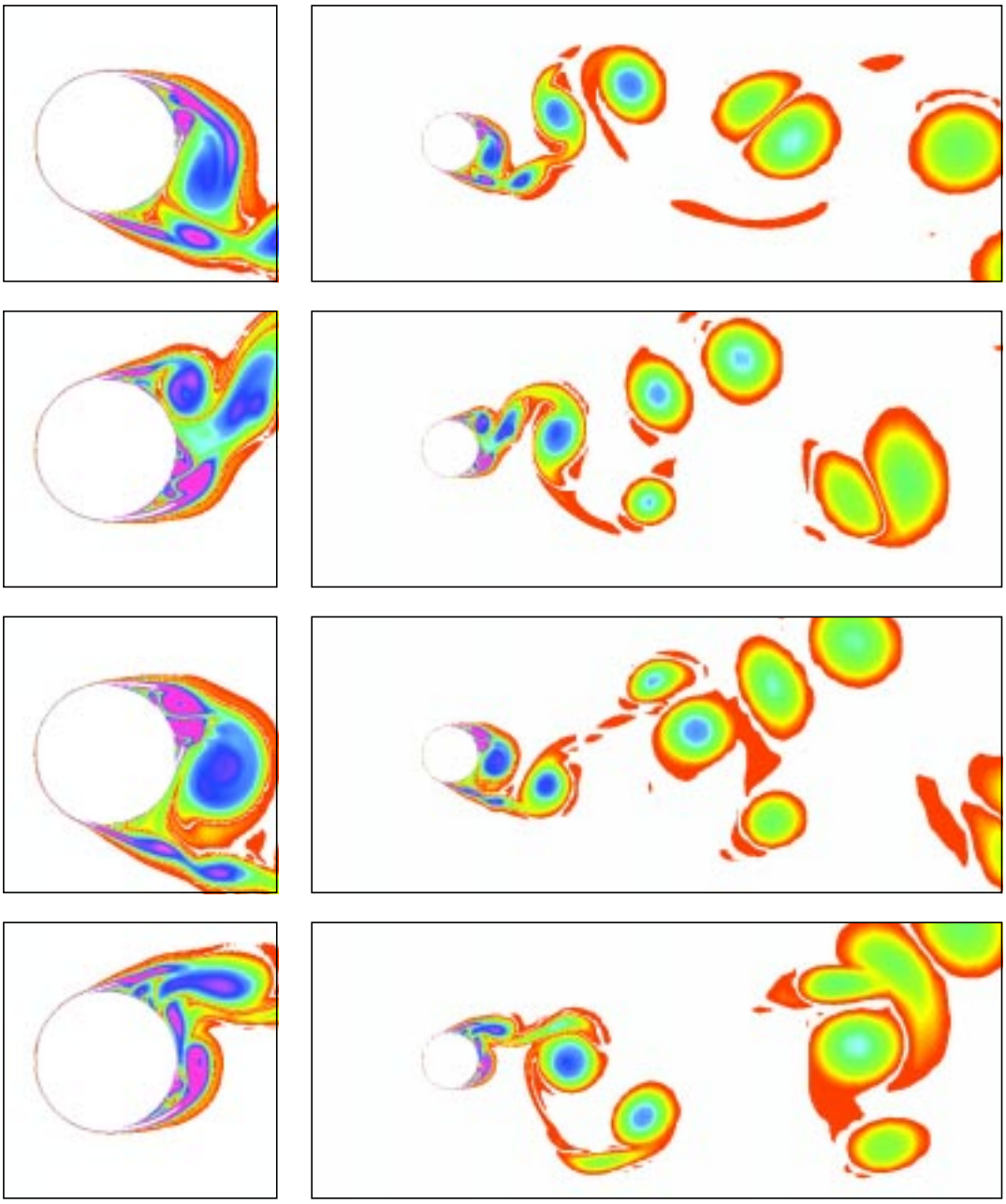

Figure 6.33. Flow past a circular cylinder at Reynolds number 10,000: vorticity field at $t = 50$, 55, 60, and 65.

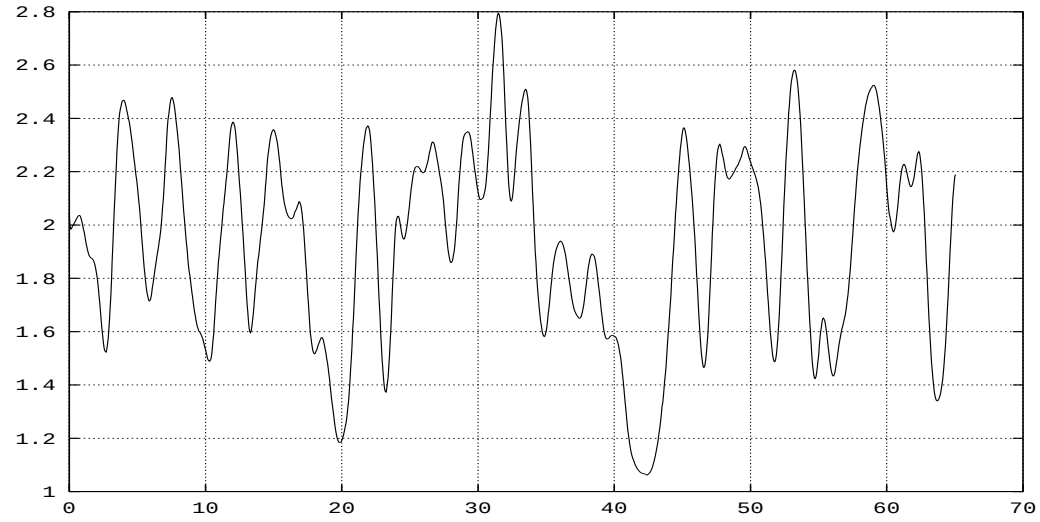

Figure 6.34. Flow past a circular cylinder at Reynolds number 10,000: time history of the drag coefficient.

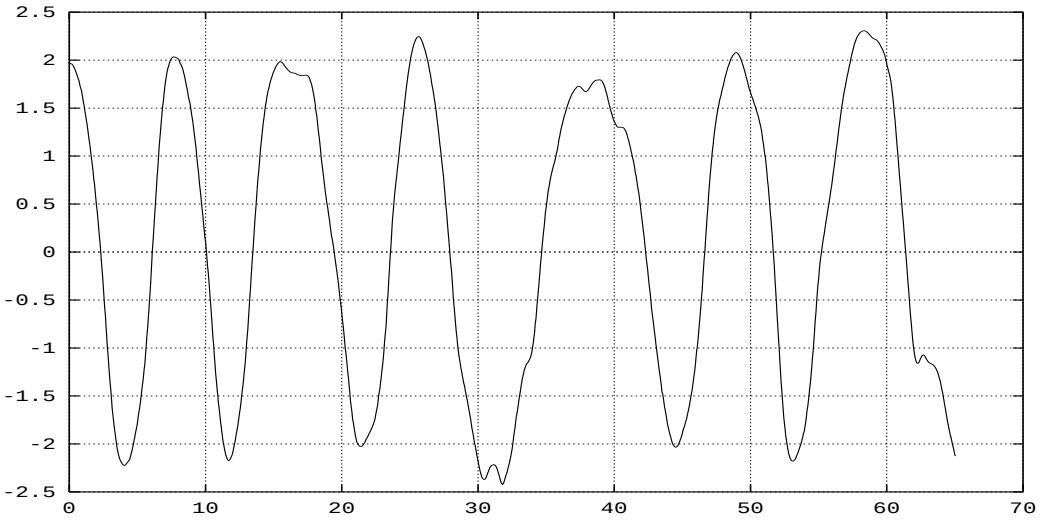

Figure 6.35. Flow past a circular cylinder at Reynolds number 10,000: time history of the lift coefficient.

6.3 Contraction of a Viscoelastic Fluid

In this section, the stress-velocity-pressure formulation is employed to simulate plane flow of a viscoelastic fluid through a 4 to 1 contraction. This problem has been used by other finite element researchers as a test case for viscoelastic formulations [37, 39]. The problem may be stated as follows:

- An Oldroyd-B fluid flows through a contracting pipe which is shown in Figure 6.36. At the inflow boundary Γ_{in} we specify a fully developed (parabolic) velocity and extra stress profiles with unit maximum velocity. The lower boundary Γ_{lower} is a no-slip surface, while the upper boundary Γ_{upper} is taken as a flow symmetry line. A fully developed velocity profile is also specified at the downstream boundary Γ_{out}. The half-width and length are 4 and 8, respectively, for the wide conduit and 1 and 5 downstream of the contraction.

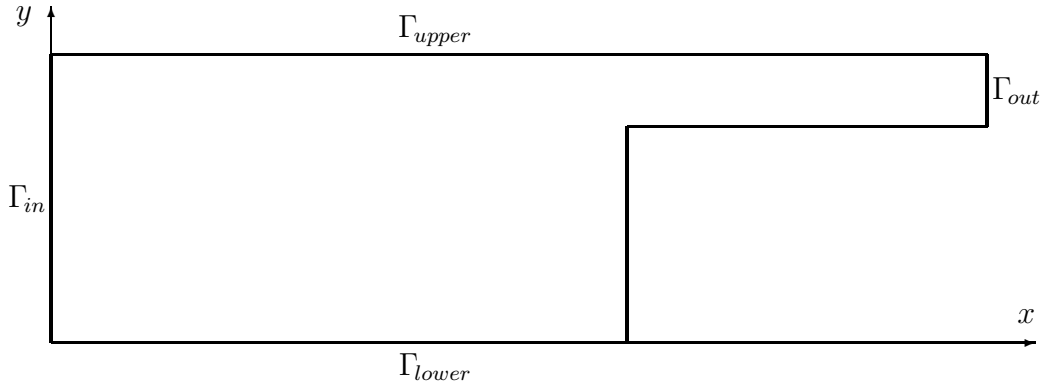

Figure 6.36. Contraction of a viscoelastic fluid: domain description.

- The viscosity of the Oldroyd-B fluid is taken as $\mu = 0.5$, with $\mu_1 = 0.445$ and $\mu_2 = 0.055$. The flow is assumed to be creeping and steady. The Deborah number is based on the wall shear rate at the outlet for a fully developed profile there $De = \lambda\gamma_{wall}$. In the present case $\gamma_{wall} = 8.0$.

- A mesh with 1,225 nodes and 1,140 elements is used, as shown in Figure 6.37. This is the same mesh as the mesh B used in [39]. Future simulations will have

to take into account the possibility of an asymmetric time dependent flow fields with respect to the centerline, which now forms the upper boundary.

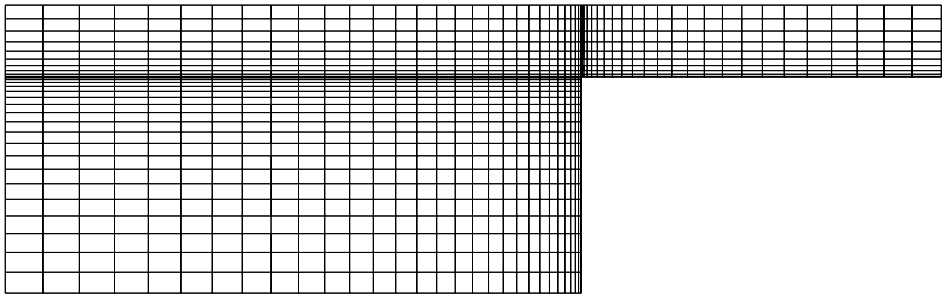

Figure 6.37. Contraction of a viscoelastic fluid: finite element mesh.

- All the cases discussed here were computed using a direct solver. The computations were performed in 64-bit precision on the Cray-XMP machine.

In Figures 6.38–6.41 we present the flow fields for $De = 0.0$ (Newtonian fluid), $De = 0.8$, $De = 1.6$ and $De = 3.2$. The first two viscoelastic cases are the subject of investigation also in [39]. In the figures we show the three components of $\mathbf{T}_1$, streamlines, velocity vectors and the pressure field. The primary variables, i.e., velocity and pressure, remain relatively insensitive to the increase in viscoelastic character of the fluid. The one visible change in the flow features is the slight expansion of the recirculation region in the corner upstream of the contraction. The normal stress fields on the other hand are visibly advected downstream. At $De = 3.2$, there are indications that the outflow boundary condition presents a difficulty. This should not influence greatly the flow field in the region of interest, i.e. near the singularity. However, in future simulations, the domain will have to be extended significantly farther downstream. The convergence at the higher values of the Deborah numbers is achieved only through a careful continuation process, restarting from converged result at a lower value of De. This is roughly equivalent to reaching the steady state as a limit of a time dependent solution, as it is done in [37, 39]. We didn't continue the computations past $De = 4.0$, because of the increasing irregularities near the outlet.

In order to compare the results with the ones obtained through the use of compatible interpolations for all variables, we also plot the sections of the stress field along the $y = 3.0$ line which is passing through the singularity. The normal stress component $\mathbf{T}_{1xx}$ for the four cases is shown in Figure 6.42. Non-dimensionalizing the stress with $\mu_1\gamma_{wall}$ we obtain a maximum of 6.17 and 9.08 for $De = 0.8$ and $De = 1.6$, compared to the corresponding maxima of 7.5 and 11.25 obtained in [39]. The stress discontinuity is relatively free of oscillations, with only one undershoot seen upstream of the contraction.

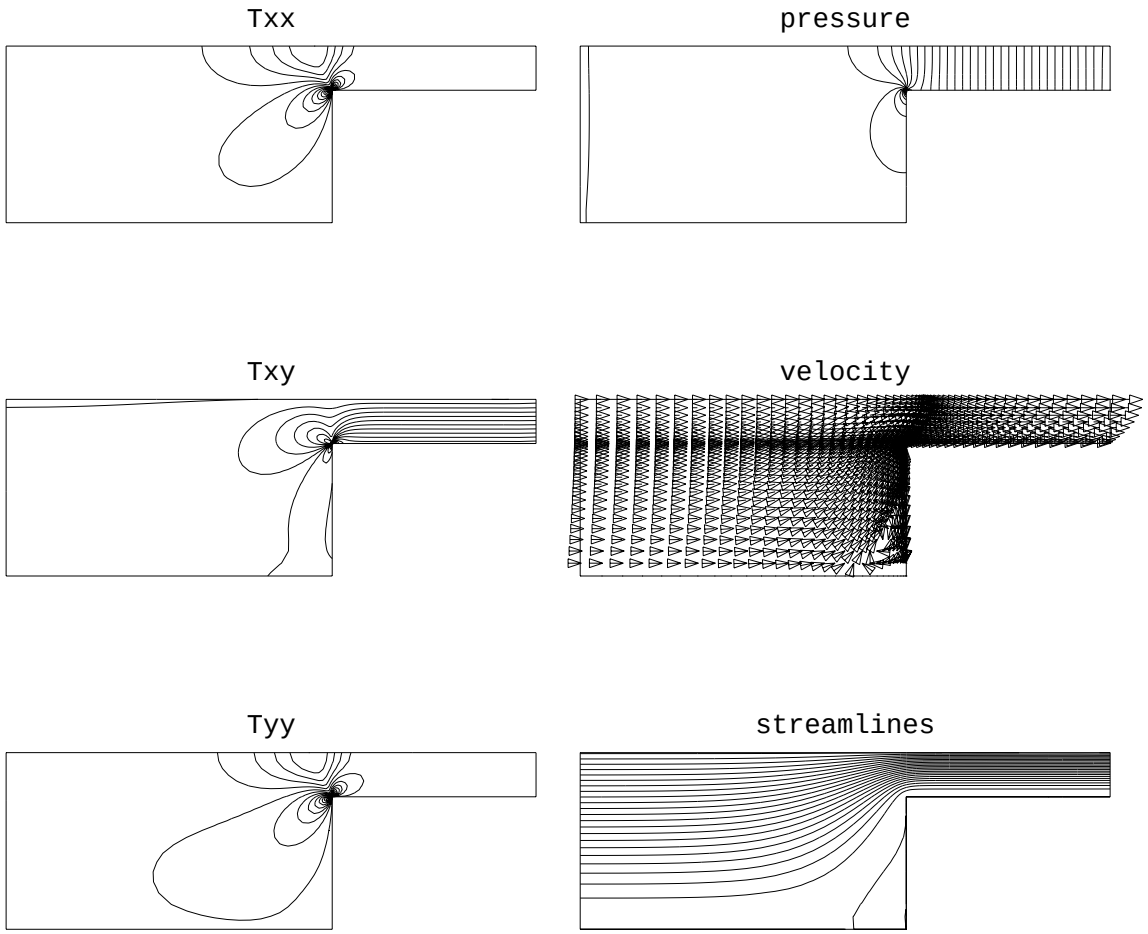

Figure 6.38. Contraction of a viscoelastic fluid: $De = 0.0$ case.

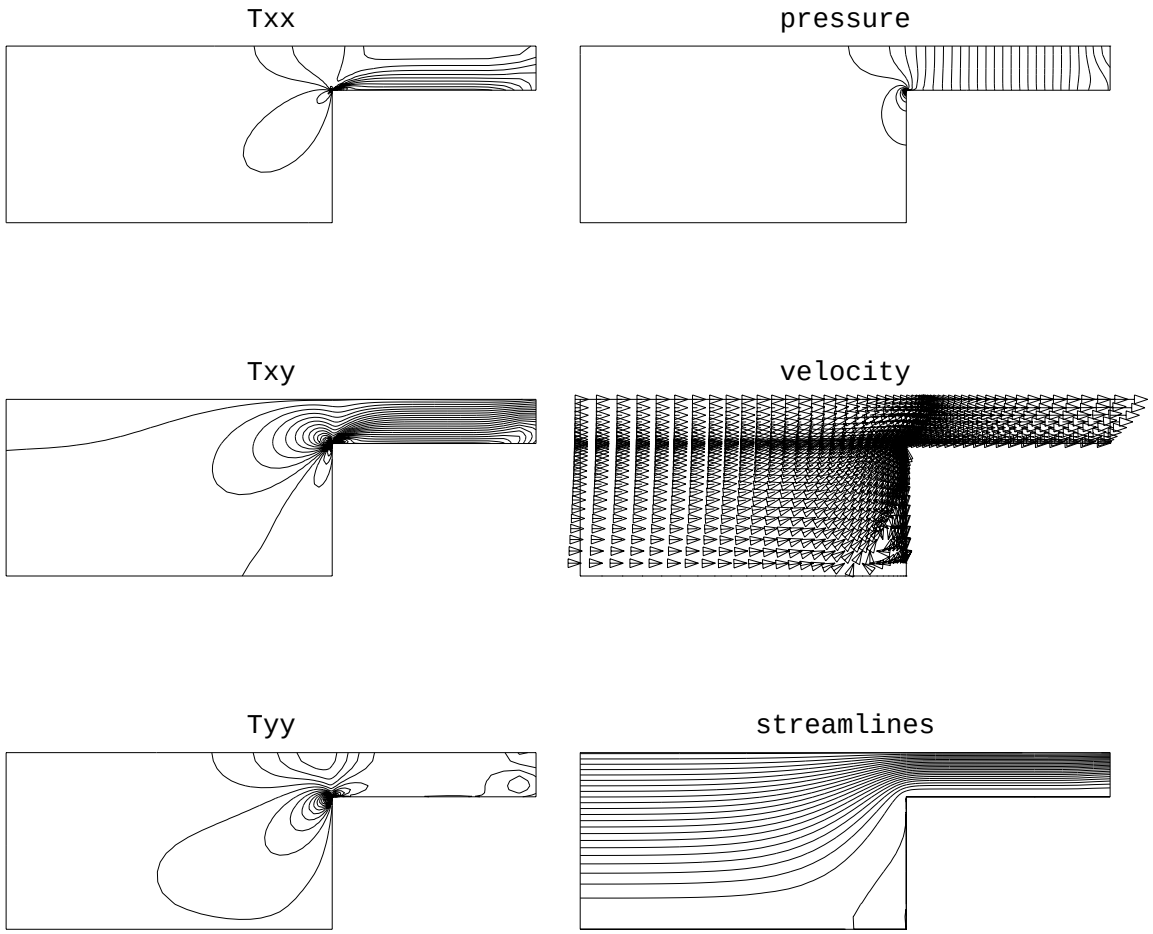

Figure 6.39. Contraction of a viscoelastic fluid: $De = 0.8$ case.

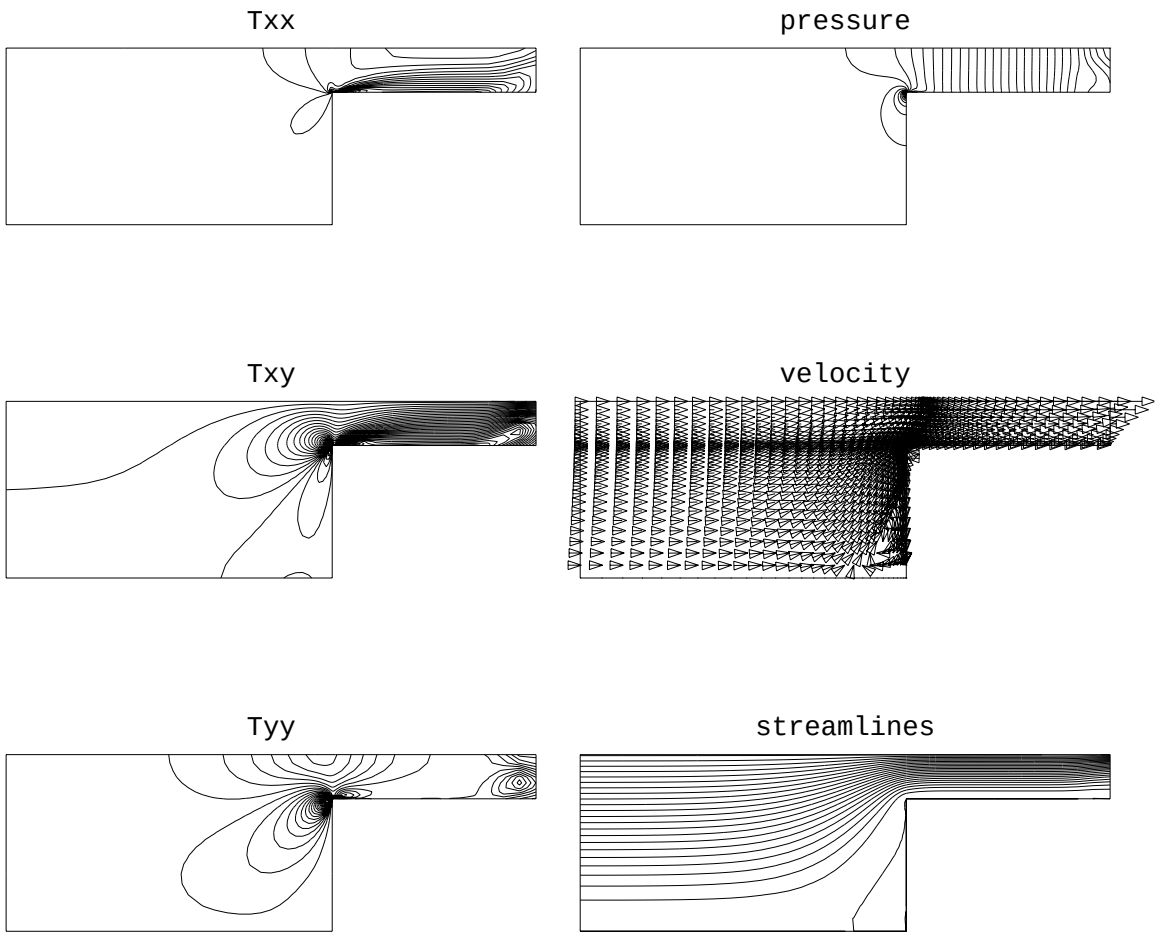

Figure 6.40. Contraction of a viscoelastic fluid: $De = 1.6$ case.

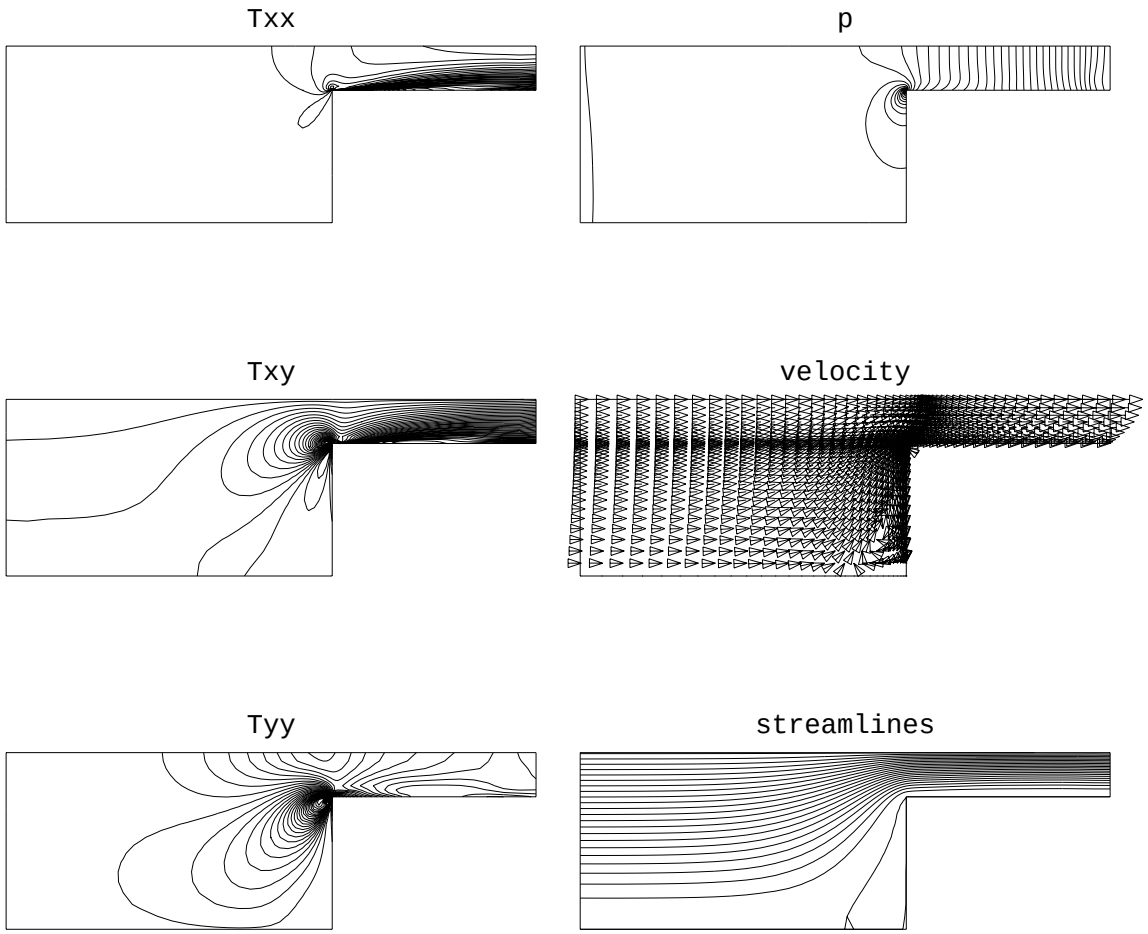

Figure 6.41. Contraction of a viscoelastic fluid: $De = 3.2$ case.

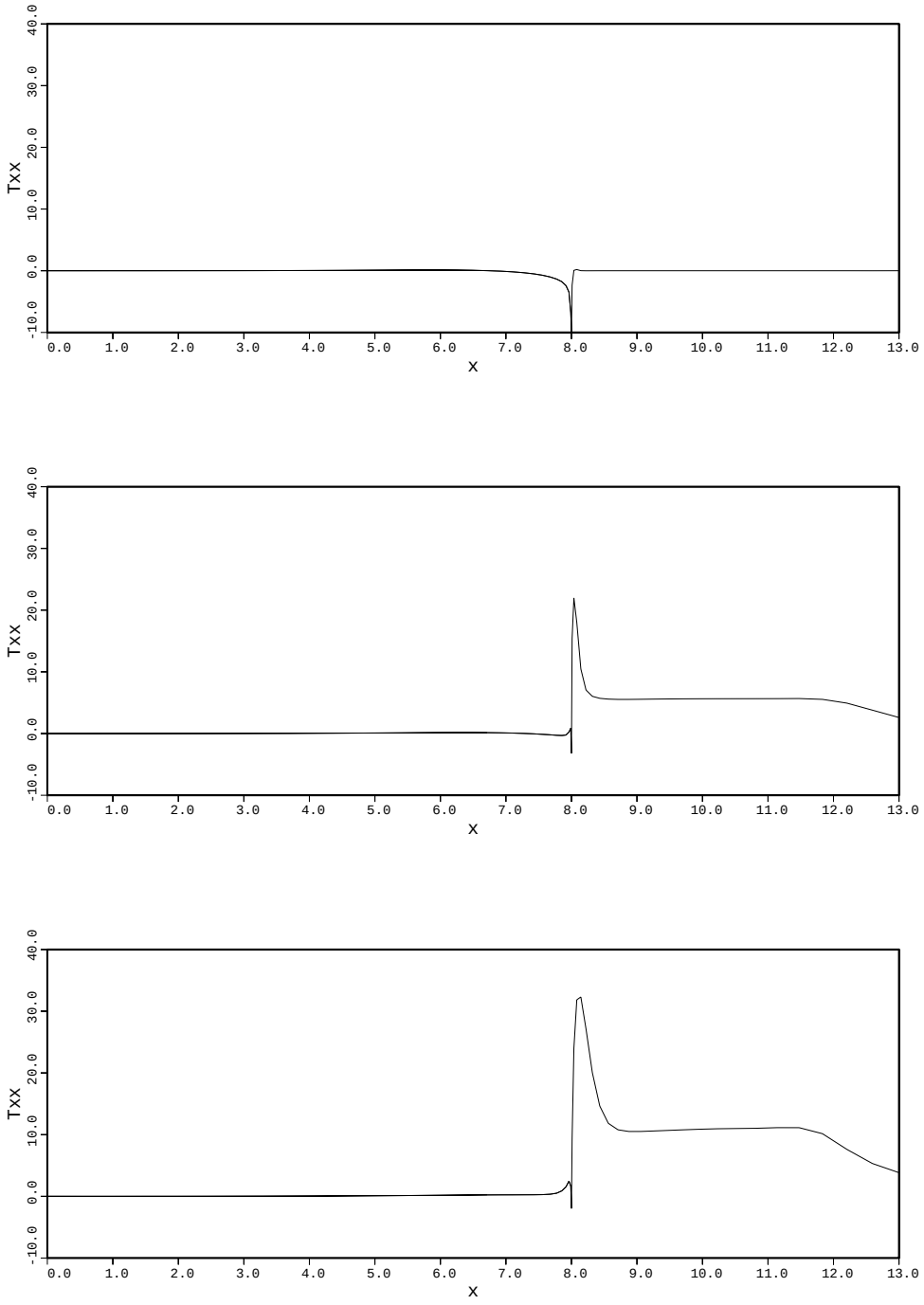

Figure 6.42. Contraction of a viscoelastic fluid: $\mathbf{T}_{1xx}$ profiles along the $y = 3.0$ line for (from top to bottom) $De = 0.0$, $De = 0.8$, $De = 1.6$ and $De = 3.2$.

Chapter 7

Conclusions

Our aim was to gain more understanding of the issues involved in numerical simulation of incompressible flows with a finite element method. The work concentrated on mixed formulations circumventing the Babuška-Brezzi condition.

We began by introducing the governing equations of the physical problem, including the incompressible Navier-Stokes equations, with a range of boundary conditions. Both Newtonian and non-Newtonian constitutive equations were given. The latter included upper-convected Maxwell and Oldroyd models characterizing the behavior of viscoelastic fluids.

We proceeded to consider a numerical method capable of modeling incompressible fluid flows in a deforming domain. After a review of alternative approaches, the current method has been introduced. It is based on the stabilized mixed velocity-pressure space-time formulation. The simultaneous discretization of both spatial and temporal domains via a finite element technique automatically accounts for the mesh deformation and non-zero velocities of the nodes. The interpolation functions are allowed to be discontinuous in time. The Galerkin formulation of the problem is stabilized with the least-squares form of the momentum and continuity equations. Such a stabilization enables us to use arbitrary combinations of interpolation function spaces for the velocity and pressure, and provides stability in the presence of sharp boundary layers, as well as at high Reynolds numbers. The method gives us substantial latitude re-

garding the movement of the mesh inside the domain, and to some extent, also at the surface. We outlined several mesh moving strategies available to us in this respect. As a first illustration, we presented a problem involving extremely large deformation of the initial domain. We deferred the demonstration of the mesh moving strategy applicable to modestly deforming domains to a dedicated chapter discussing other numerical examples. Guidelines for obtaining a matrix form of the problem were given, along with remarks about the massively parallel implementation of the matrix formation process.

In a separate development, we attempted to formulate a method capable of simulating incompressible flow of viscoelastic fluids. Currently available solutions for this task were first outlined. Then, a stabilized mixed stress-velocity-pressure formulation has been introduced. This method may be used with any combination of interpolation functions for all three fields involved. The stabilization is achieved through the addition of least-squares forms of the momentum, constitutive and continuity equations. The first provides stability in the presence of high streamwise gradients, and allows us to circumvent the compatibility condition for the velocity and pressure interpolation function spaces. The second performs a similar function for the constitutive equation, which in the case of viscoelastic fluids, acquires a transport character. This stabilizing component also removes the compatibility requirement for the velocity and stress interpolations. The final stabilization factor improves convergence at high Reynolds numbers. The temporal discretization of the method can employ either a classical α-scheme, which is used for the numerical examples presented later, or a full space-time approach.

Both formulations presented so far benefit from implicit solution techniques, which were discussed next. We started with a brief review of direct solvers, including the ideas of skyline storage, bandwidth and bandwidth reduction. Recognizing the excessive cost of the direct solution, we moved on to the iterative methods in general, and the Generalized Minimum Residual method in particular. An efficient version of that algorithm was recounted, and the issues of convergence and preconditioning touched upon. The implementation of linear equation solvers on massively parallel

computer has been a challenging topic. Here, we described our experience in this area, stemming from the implementation of the GMRES method on a data parallel architecture.

Finally, we presented the results from several computations which were performed with the aid of numerical methods described so far. The velocity-pressure space-time formulation has been used for three-dimensional simulation of large amplitude sloshing in a rectangular tank. When subjected to a horizontal excitation, the wave motion has been found to be two-dimensional and consisting of the expected first mode only. When the excitation is vertical, three-dimensional waves were observed. The stress-velocity-pressure formulation, coupled with the constitutive equations of a Newtonian fluid, was used to perform high-resolution simulations of flow past a circular cylinder at Reynolds number ranging from 1,000 to 10,000. Lastly the constitutive equation for an Oldroyd-B fluid was substituted and the same formulation was used to compute the flow of a viscoelastic fluid through a contraction.

7.1 Future Research Directions

The continuation of the work presented in this thesis is expected to include:

- The inclusion of more complete set of free surface effects, such as contact angles and surface tension in three dimensions.
- Completion of the stability and accuracy analysis for the stress-velocity-pressure method in the context of viscoelastic constitutive laws, with possible new designs for the stabilization parameter.
- Efficient implementation of the CEBE preconditioner on data parallel architectures.
- An in-depth study of wave mode competition in vertically excited rectangular and cylindrical tanks.

- Cross-reference of two-dimensional simulations of flow past a cylinder with three-dimensional ones.
- Pre- and post-processing work to improve the ability to handle three-dimensional flow computations. This includes mesh generation and visualization efforts.

Bibliography

[1] P.M. Gresho, "Incompressible fluid dynamics: Some fundamental formulation issues", *Annual Review of Fluid Mechanics*, **23** (1991) 413–453.

[2] F.H. Harlow, J.E. Welch, J.P. Shannon, and B.J. Daly, "The MAC method", Report LA-3425, Los Alamos Scientific Laboratory, 1965.

[3] B.J. Daly, "A technique for including surface tension effects in hydrodynamics calculations", *Journal of Computational Physics*, **4** (1969) 97–117.

[4] R.K.C. Chan and R.L. Street, "A computer study of finite-amplitude water waves", *Journal of Computational Physics*, **6** (1970) 68–94.

[5] C. W. Hirt and B. D. Nichols, "Volume of Fluid (VOF) method for the dynamics of free boundaries", *Journal of Computational Physics*, **39** (1981) 201–225.

[6] C.W. Hirt, J.L. Cook, and T.D. Butler, "A Lagrangian method for calculating the dynamics of an incompressible fluid with free surface", *Journal of Computational Physics*, **5** (1970) 103–124.

[7] T. Okamoto and M. Kawahara, "Two-dimensional sloshing analysis by Lagrangian finite element method", *International Journal for Numerical Methods in Fluids*, **11** (1990) 453–477.

[8] C.W. Hirt, A.A. Amsden, and J.L. Cook, "An arbitrary Lagrangian Eulerian computing method for all flow speeds", *Journal of Computational Physics*, **14** (1974) 227–253.

[9] T.J.R. Hughes, W.K. Liu, and T.K. Zimmermann, "Lagrangian-Eulerian finite element formulation for incompressible viscous flows", *Computer Methods in Applied Mechanics and Engineering*, **29** (1981) 329–349.

[10] A. Huerta and W.K. Liu, "Viscous flow with large free surface motion", *Computer Methods in Applied Mechanics and Engineering*, **69** (1988) 277–324.

[11] A. Soulaimani, M. Fortin, G. Dhatt, and Y. Ouellet, "Finite element simulation of two- and three-dimensional free surface flows", *Computer Methods in Applied Mechanics and Engineering*, **86** (1991) 265–296.

[12] P. Jamet and R. Bonnerot, "Numerical solution of the Eulerian equations of compressible flow by a finite element method which follows the free boundary and the interfaces", *Journal of Computational Physics*, **18** (1975) 21–45.

[13] R. Bonnerot and P. Jamet, "Numerical computation of the free boundary for the two-dimensional Stefan problem by space-time finite elements", *Journal of Computational Physics*, **25** (1977) 163–181.

[14] D.R. Lynch and W.G. Gray, "Finite element simulation of flow in deforming regions", *Journal of Computational Physics*, **36** (1980) 135–153.

[15] C.S. Frederiksen and A.M. Watts, "Finite-element method for time-dependent incompressible free surface flows", *Journal of Computational Physics*, **39** (1981) 282–304.

[16] P. Jamet, "Galerkin-type approximations which are discontinuous in time for parabolic equations in a variable domain", *SIAM Journal of Numerical Analysis*, **15** (1978) 912–928.

[17] T.J.R. Hughes and G.M. Hulbert, "Space-time finite element methods for elastodynamics: formulations and error estimates", *Computer Methods in Applied Mechanics and Engineering*, **66** (1988) 339–363.

[18] P. Hansbo and A. Szepessy, "A velocity-pressure streamline diffusion finite element method for the incompressible Navier-Stokes equations", *Computer Methods in Applied Mechanics and Engineering*, **84** (1990) 175–192.

[19] T.E. Tezduyar, M. Behr, and J. Liou, "A new strategy for finite element computations involving moving boundaries and interfaces – the deforming-spatial-domain/space-time procedure: I. The concept and the preliminary tests", *Computer Methods in Applied Mechanics and Engineering*, **94** (1992) 339–351.

[20] T.E. Tezduyar, M. Behr, S. Mittal, and J. Liou, "A new strategy for finite element computations involving moving boundaries and interfaces – the deforming-spatial-domain/space-time procedure: II. Computation of free-surface flows, two-liquid flows, and flows with drifting cylinders", *Computer Methods in Applied Mechanics and Engineering*, **94** (1992) 353–371.

[21] M. Behr, A. Johnson, J. Kennedy, S. Mittal, and T.E. Tezduyar, "Computation of incompressible flows with implicit finite element implementations on the Connection Machine", *Computer Methods in Applied Mechanics and Engineering*, **108** (1993) 99–118.

[22] T.E. Tezduyar, M. Behr, S. Mittal, and A.A. Johnson, "Computation of unsteady incompressible flows with the finite element methods – space-time formulations, iterative strategies and massively parallel implementations", in P. Smolinski, W.K. Liu, G. Hulbert, and K. Tamma, editors, *New Methods in Transient Analysis*, AMD-Vol.143, ASME, New York, (1992) 7–24.

[23] S. Mittal and T.E. Tezduyar, "A finite element study of incompressible flows past oscillating cylinders and airfoils", *International Journal for Numerical Methods in Fluids*, **15** (1992) 1073–1118.

[24] S. Mittal, *Stabilized Space-Time Finite Element Formulations for Unsteady Incompressible Flows Involving Fluid-Body Interactions*, Ph.D. thesis, Department of Aerospace Engineering and Mechanics, University of Minnesota, 1992.

[25] P. Hansbo, "The characteristic streamline diffusion method for the time-dependent incompressible Navier-Stokes equations", *Computer Methods in Applied Mechanics and Engineering*, **99** (1992) 171–186.

[26] S. Aliabadi and T.E. Tezduyar, "Space-time finite element computation of compressible flows involving moving boundaries and interfaces", *Computer Methods in Applied Mechanics and Engineering*, **107** (1993) 209–224.

[27] J.P. Benque, A. Haugel, and P.L. Viollet, "Numerical methods in environmental fluid mechanics", in M.B. Abbott and J.A. Cunge, editors, *Engineering Applications of Computational Hydraulics*, volume II, Pitman, 1982.

[28] A.N. Brooks and T.J.R. Hughes, "Streamline upwind/Petrov-Galerkin formulations for convection dominated flows with particular emphasis on the incompressible Navier-Stokes equations", *Computer Methods in Applied Mechanics and Engineering*, **32** (1982) 199–259.

[29] F. Brezzi and J. Pitkäranta, "On the stabilization of finite element approximations of the Stokes problem", in W. Hackbusch, editor, *Efficient Solutions of Elliptic Systems*, volume 10 of *Notes on Numerical Fluid Mechanics*, 11–19, Vieweg, Wiesbaden, 1984.

[30] T.J.R. Hughes, L.P. Franca, and M. Balestra, "A new finite element formulation for computational fluid dynamics: V. Circumventing the Babuška–Brezzi condition: A stable Petrov–Galerkin formulation of the Stokes problem accommodating equal-order interpolations", *Computer Methods in Applied Mechanics and Engineering*, **59** (1986) 85–99.

[31] T.E. Tezduyar, S. Mittal, S.E. Ray, and R. Shih, "Incompressible flow computations with stabilized bilinear and linear equal-order-interpolation velocity-pressure elements", *Computer Methods in Applied Mechanics and Engineering*, **95** (1992) 221–242.

[32] L.P. Franca and T.J.R. Hughes, "Two classes of mixed finite element methods", *Computer Methods in Applied Mechanics and Engineering*, **69** (1988) 89–129.

[33] L.P. Franca and S.L. Frey, "Stabilized finite element methods: II. The incompressible Navier-Stokes equations", *Computer Methods in Applied Mechanics and Engineering*, **99** (1992) 209–233.

[34] M. Behr, L.P. Franca, and T.E. Tezduyar, "Stabilized finite element methods for the velocity-pressure-stress formulation of incompressible flows", *Computer Methods in Applied Mechanics and Engineering*, **104** (1993) 31–48.

[35] F. Hecht and E. Satel, "Emc^2 un logiciel d'édition de maillages et de contours bidimensionnels", RT n^{o}118, INRIA, April 1990.

[36] T.J.R Hughes, *The Finte Element Method. Linear Static and Dynamic Finite Element Analysis*. Prentice-Hall, Englewood Cliffs, New Jersey, 1987.

[37] J. M. Marchal and M. J. Crochet, "A new mixed finite element for calculating viscoelastic flow", *Journal of Non-Newtonian Fluid Mechanics*, **26** (1987) 77–114.

[38] R. Keunings, "On the high Weissenberg number problem", *Journal of Non-Newtonian Fluid Mechanics*, **20** (1986) 209–226.

[39] M. Fortin and A. Fortin, "A new approach for the FEM simulation of viscoelastic flows", *Journal of Non-Newtonian Fluid Mechanics*, **32** (1989) 295–310.

[40] G.C. Georgiou and M.J. Crochet, "The simultaneous use of 4×4 and 2×2 bilinear stress elements for viscoelastic flows", to appear in *Journal of Computational Mechanics*, 1992.

[41] A. Fortin and M. Fortin, "A preconditioned generalized minimum residual algorithm for the numerical solution of viscoelastic fluid flows", *Journal of Non-Newtonian Fluid Mechanics*, **36** (1990) 277–288.

[42] E. Cuthill and J. McKee, "Reducing the bandwidth of sparse symmetric matrices", in *Proceedings of 24th National Conference of the ACM*, volume P-69, (1969) 157–172.

[43] J.A. George, "Computer implementation of the finite element method", Technical Report STAN-CS-71-208, Computer Science Department, Stanford University, Stanford, California, 1971.

[44] D.M. Young, "A historical overview of iterative methods", *Computer Physcis Communications*, **53** (1989) 1–17.

[45] Y. Saad and M. Schultz, "GMRES: A generalized minimal residual algorithm for solving nonsymmetric linear systems", *SIAM Journal of Scientific and Statistical Computing*, **7** (1986) 856–869.

[46] Y. Saad, "A flexible inner-outer preconditioned GMRES algorithm", *SIAM Journal on Scientific Computing*, **14** (1993) 461–469.

[47] T.E. Tezduyar, M. Behr, S.K. Aliabadi, S. Mittal, and S.E. Ray, "A new mixed preconditioning method for finite element computations", *Computer Methods in Applied Mechanics and Engineering*, **99** (1992) 27–42.

[48] Y. Saad, "Krylov subspace methods for solving large unsymmetric linear systems", *Mathematics of Computation*, **37** (1981) 105–126.

[49] T.J.R. Hughes, J. Winget, I. Levit, and T.E. Tezduyar, "New alternating direction procedures in finite element analysis based upon EBE approximate factorizations", in S. Atluri and N. Perrone, editors, *Recent Developments in Computer Methods for Nonlinear Solid and Structural Mechanics*, 75–109, ASME, 1983.

[50] J. Liou and T.E. Tezduyar, "Computation of compressible and incompressible flows with the clustered element-by-element method", Research Report UMSI 90/215, University of Minnesota Supercomputer Institute, 1200 Washington Avenue South, Minneapolis, MN 55415, October 1990.

[51] J. Liou and T.E. Tezduyar, "A clustered element-by-element iteration method for finite element computations", in R. Glowinski et al., editor, *Domain Decomposition Methods for Partial Differential Equations*, Chapter 13, 140–150, SIAM, 1991.

[52] Z. Johan, *Data Parallel Finite Element Techniques for Large-Scale Computational Fluid Dynamics*, Ph.D. thesis, Department of Mechanical Engineering, Stanford University, 1992.

[53] K. Muto, Y. Kasai, M. Nakahara, and Y. Ishida, "Experimental tests on sloshing response of a water pool with submerged blocks", in S.J. Brown, editor, *Proceedings of the 1985 Pressure Vessels and Piping Conference 98-7 (Fluid Structure Dynamics)*. ASME, (1985) 209–214.

[54] M.S. Engelman, R.L. Sani, and P.M. Gresho, "The implementation of normal and/or tangential boundary conditions in finite element codes for incompressible fluid flow", *International Journal for Numerical Methods in Fluids*, **2** (1982) 225–238.

[55] F. Simonelli and J.P. Gollub, "Surface wave mode interactions: Effects of symmetry and degeneracy", *Journal of Fluid Mechanics*, **199** (1989) 471–494.

[56] Z.C. Feng and P.R. Sethna, "Symmetry-breaking bifurcations in resonant surface waves", *Journal of Fluid Mechanics*, **199** (1989) 495–518.

[57] H. Schlichting, *Boundary-Layer Theory*. McGraw-Hill, New York, 7 edition, 1979.

[58] M. Braza, P. Chassaing, and H. Ha Minh, "Numerical study and physical analysis of the pressure and velocity fields in the near wake of a circular cylinder", *Journal of Fluid Mechanics*, **165** (1986) 79–130.

[59] M. Tabata and S. Fujima, "An upwind finite element scheme for high-Reynolds-number flows", *International Journal for Numerical Methods in Fluids*, **12** (1991) 305–322.

[60] M. Tabata and S. Fujima, "Finite element analysis of a high-Reynolds-number flow problem", preprint, July 1990.

[61] A. Kourta, H.C. Boisson, P. Chassaing, and H. Ha Minh, "Nonlinear interaction and the transition to turbulence in the wake of a circular cylinder", *Journal of Fluid Mechanics*, **181** (1987) 141–161.